THE UNIVERSITY OF CHICAGO

A SEARCH FOR NEW PHYSICS IN PHOTON-LEPTON EVENTS IN PROTON-ANTIPROTON COLLISIONS AT $\sqrt{S} = 1.8$ TEV

A DISSERTATION SUBMITTED TO
THE FACULTY OF THE DIVISION OF THE PHYSICAL SCIENCES
IN CANDIDACY FOR THE DEGREE OF
DOCTOR OF PHILOSOPHY

DEPARTMENT OF PHYSICS

BY
JEFFREY W. BERRYHILL

CHICAGO, ILLINOIS
DECEMBER 2000

ABSTRACT

We present the results of a search in $p\bar{p}$ collisions at $\sqrt{s} = 1.8$ TeV for anomalous production of events containing a photon with large transverse energy and a lepton (e or μ) with large transverse energy, using 86 pb^{-1} of data collected at the Collider Detector at Fermilab during the 1994-95 collider run at the Fermilab Tevatron. The presence of large missing transverse energy ($\not\!\!E_{\rm T}$), additional photons, or additional leptons in these events is also analyzed. The results are consistent with standard model expectations, with the possible exception of photon-lepton events with large $\not\!\!E_{\rm T}$, for which the probability of a statistical fluctuation of the standard model expectation up to and above the observed level is 0.7%.

ACKNOWLEDGMENTS

Successful doctoral candidates owe their accomplishments to a vast network of supporters: mentors, colleagues, assistants, friends, and loved ones. In this small space I shall attempt to enumerate them and their virtues. It is a list which is undoubtedly incomplete and expresses but a fraction of the gratitude owed to my benefactors.

Henry Frisch was my chief advisor, teacher, mentor, and motivator. He dared me to take on the most challenging projects (the subject of this dissertation was largely taken up on a dare), and never doubted that I would be successful. If I did not disagree with him so often, I wouldn't be half the scientist I am today. Obversely, Melvyn Shochet was an inexhaustible source of scientific knowledge and advice. There is much to be learned from following his example, which is simply to know everything.

Harold Sanders enabled me to learn the art of digital electronic design. I started as someone who knew absolutely nothing working on a project that would be difficult for experts; we finished with a successful design that won a professional award. Ray Culbertson, William Ashmanskas, and Mircea Bogdan also assisted me with design, and ultimately turned that design into a working reality for future CDF experiments.

Ray Culbertson and Peter Wilson studied photons alongside me in Chicago and contributed to the techniques used here. They inspired me to behave more like a postdoctoral researcher than a graduate student. David Toback and John Wahl were my CDF student friends and compatriots in Chicago for many years. They knew the indispensable details that only graduate students know, and gave me the sympathy and the moral support only graduate students can give.

A number of physicists elsewhere went out of their way to help me with this topic of research. Pasha Murat was a very busy CDF collaborator who was among the few in CDF to actively assist me in my analysis. Uli Baur and Stephen Mrenna offered a great deal of help in the form of providing me with physics simulation software and answering my many questions about the theoretical details. Jon Rosner and Troy Andre took interest in the details of my research and offered their assistance despite their responsibilities in theoretical research.

Besides those who actively helped me, there are hundreds of CDF, Fermilab, Enrico Fermi Institute, and Physics Department employees and collaborators without whom a graduate education from a grand scientific enterprise, such as experimental high energy physics, simply would not exist. Among them, Kathy Visak of the Enrico Fermi Institute and Nobuko McNeill of the Physics Department were of valuable assistance to me in navigating the many administrative obstacles all graduate students must surmount. Marty Dippel tirelessly maintained the archaic DEC computers on which I relied; we shall raise many toasts upon my graduation and the subsequent retirement of those machines.

To my fellow graduate students in the physics department, Eric Zimmermann, Joseph Fowler, Theodore Quinn, James Geddes, Jordan Koss, Gavin Polhemus, and others: your friendship, intellectual companionship, and mutual support in our endeavors is highly treasured. Convening regularly at the Medici for lunch or the Pub for a beer helped to remind me of the priorities and benefits of friendship. David and Sharon Berryhill, my loving parents, unceasingly encouraged me in the pursuit of my educational goals, wherever it took me. Last but not least, Nancy Floriant, you brightened my world even in the darkest of moments, and I could not have made it through without you.

For those left unacknowledged, I invite you to imagine the universal love for mankind one experiences only upon completion of the most arduous and rewarding of achievements: that is what I feel for you.

TABLE OF CONTENTS

LIST OF FIGURES

LIST OF TABLES

CHAPTER 1

INTRODUCTION

An important test of the standard model of particle physics (and the extent of its validity) is to measure and understand the properties of the highest energy particle collisions. The chief predictions of the standard model for these collisions are the numbers and varieties of fundamental particles, i.e., the fermions and gauge bosons of the standard model, that are produced. The chief indicators of new physical processes must therefore include the production rates of any combinations of such particles. This paper describes an analysis of the production of a set of combinations involving at least one photon and at least one lepton (e or μ), using 86 pb^{-1} of data from proton-antiproton collisions collected at the Collider Detector at Fermilab (CDF) [1] during the 1994-95 run of the Fermilab Tevatron.

Production of these particular combinations of particles is of interest for several reasons. Events with photons and leptons are potentially related to the unexplained $ee\gamma\gamma\not{E}_{\rm T}$ event recorded by CDF [2]. A supersymmetric model [3] designed to explain the $ee\gamma\gamma\not{E}_{\rm T}$ event predicts the production of photons from the radiative decay of the $\tilde{\chi}_2^0$ neutralino, and leptons through the decay of charginos, indicating $\ell\gamma\not{E}_{\rm T}$ events as a signal for gaugino pair production. Other hypothetical, massive particles beyond those in the standard model will typically cascade decay to one or more electroweak gauge bosons, one of which could be a photon and the other of which could be a leptonically decaying W or Z^0 boson. In addition, photon-lepton studies complement similarly motivated inclusive searches for new physics in diphoton [4], photon-jet [5], and photon-b-quark events [6].

The scope and strategy of this analysis are meant to reflect the motivating principles. Categories of photon-lepton events are defined *a priori* in a way that characterizes the different possibilities for new physics, inclusive event rates are compared with standard model expectations, and a few simple kinematic distributions are presented for further examination. The decay products of massive particles are typically isolated from other particles, and possess large transverse momentum and low rapidity; therefore the search is initially limited to those events with at least one isolated, central ($|\eta| < 1.0$) photon with $E_T > 25$ GeV, and at least one isolated, central electron or muon with $E_T > 25$ GeV. Studying this class of events has the added advantage of highly efficient detection and data acquisition. These photon-lepton candidates are further partitioned by angular separation. Events where exactly one photon and one lepton are detected nearly opposite in azimuth ($\Delta\varphi_{\ell\gamma} > 150^\circ$) are characteristic of a two-particle final state (two-body photon-lepton events), and the remaining photon-lepton events are characteristic of three or more particles in the final state (multi-body photon-lepton events). The inclusive event rates and properties are studied for each of these two categories. The multi-body photon-lepton events are then further studied for the presence of additional particles: photons, leptons, or the missing transverse energy associated with weakly interacting neutral particles.

Chapter 2 describes the CDF detector. Chapter 3 specifies the methods for identifying photons and leptons, and the selection of photon-lepton candidates. Chapter 4 estimates the standard model sources of photon-lepton candidates in the various search categories. Chapter 5 compares the standard model expectations with the CDF data. Chapter 6 presents the conclusions of the analysis.

CHAPTER 2

THE CDF DETECTOR

The CDF detector is an azimuthally symmetric, forward-backward symmetric particle detector designed to study $\bar{p}p$ collisions at the Fermilab Tevatron. A schematic drawing of the major detector components is shown in Figure 2.1. A superconducting solenoid of length 4.8 m and radius 1.5 m generates a 1.4 T magnetic field and contains tracking chambers used to detect charged particles and measure their momenta. Sampling calorimeters, used to measure the electromagnetic and hadronic energy deposited by electrons, photons, and jets of hadrons, surround the solenoid. Outside the calorimeters are drift chambers used for muon detection. In this section the subsystems relevant to this analysis are briefly described; a more detailed description can be found elsewhere [1].

A set of vertex time projection chambers (VTX) [7] provides measurements in the r-z plane up to a radius of 22 cm and detects particle tracks in the region $|\eta| < 3.25$. VTX tracks are used to find the z position of the $\bar{p}p$ interaction (z_{event}) and to constrain the origin of track helices. The 3.5 m long central tracking chamber (CTC) is a wire drift chamber which provides up to 84 measurements between the radii of 31.0 cm and 132.5 cm, efficient for track detection in the region $|\eta| < 1.0$. The CTC measures the momenta of charged particles with momentum resolution $\sigma_p/p < 0.0011p$, where p is measured in in GeV/c.

The calorimeter, constructed of projective electromagnetic and hadronic towers, is divided into three separate η regions: a central barrel which surrounds the

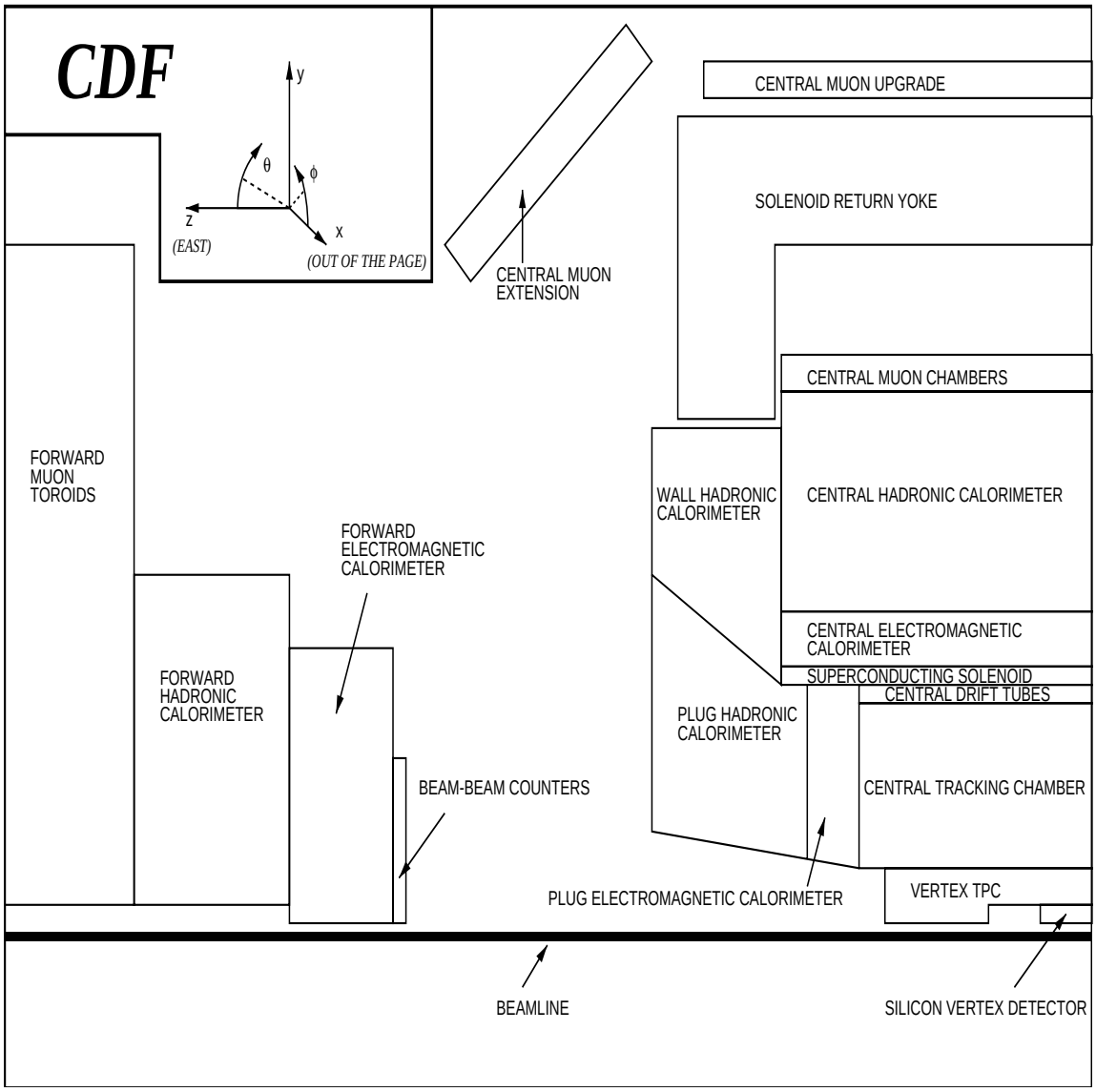

Figure 2.1: A schematic drawing of one quadrant of the CDF detector.

solenoid coil ($|\eta| < 1.1$), 'end-plugs' ($1.1 < |\eta| < 2.4$), and forward/backward modules ($2.4 < |\eta| < 4.2$). The central barrel has an electromagnetic calorimeter (CEM) which measures the total energy of electrons and photons, as well as measuring a portion of the energies of penetrating hadrons and muons. The CEM is a sampling calorimeter consisting of polystyrene scintillator sandwiched between lead absorber sheets, and is segmented into 480 towers spanning 15° in φ and 0.1 in η. The CEM is also instrumented with proportional chambers (CES) embedded near shower maximum at approximately 6 radiation lengths. Wires and cathode strips in the CES measure electromagnetic shower profiles in the φ and z views, respectively. Beyond the outer radius of the CEM is a hadronic calorimeter (CHA) which absorbs and measures the energy of hadrons, as well as a portion of the energy of penetrating muons. The CHA is a sampling calorimeter consisting of acrylic scintillator sandwiched between iron absorber sheets, and is segmented similarly to the CEM. An endwall hadronic calorimeter (WHA) covers the gap between the central barrel calorimetry and the end-plug calorimetry, with construction similar to the CHA. The end-plug calorimeters, one on each side of the central barrel, have an electromagnetic calorimeter (PEM) consisting of proportional chambers sandwiched between lead absorber sheets, and a hadronic calorimeter (PHA) consisting of proportional chambers sandwiched between iron absorber sheets. The PEM and PHA are both segmented into towers spanning 5° in φ and 0.09 in η. The forward/backward modules also have electromagnetic (FEM) and hadronic (FHA) calorimeters, and are constructed similarly to the PEM and PHA.

Muons are detected with three systems of muon chambers situated outside the calorimeters in the region $|\eta| < 1.1$. The central muon detector (CMU) system consists of four layers of drift chambers directly outside the central hadronic calorimeter,

covering 84% of the solid angle for $|\eta| < 0.6$. The central muon upgrade (CMP) system is an additional four layers of drift chambers located behind 0.6 m of steel, covering 63% of the solid angle for $|\eta| < 0.6$. About 53% of the solid angle for $|\eta| < 0.6$ is covered by both the CMU and the CMP. The central muon extension (CMX) system consists of four layers of drift tubes sandwiched between scintillation counters. The CMX detector covers 71% of the solid angle for $0.6 < |\eta| < 1.0$. In each muon system the drift chambers reconstruct the position of charged particles using the time-to-distance relationship in the transverse $(r - \varphi)$ plane, and charge division in the longitudinal $(r - z)$ plane. Three-dimensional muon track segments ("muon stubs") consist of position measurements in at least three out of the four layers of chambers, in both the $r - \varphi$ and $r - z$ planes.

A three-level multipurpose trigger is used to select $p\bar{p}$ collisions for analysis. Each level is a logical `OR` of a number of triggers designed to select events with electrons, muons, photons, or jets. The function of each trigger level is briefly described here; the particular trigger combinations employed in this analysis are specified in Chapter 3.

The first trigger stage, "Level 1", uses fast outputs from the three central muon detectors for muon triggers, and fast outputs from all the calorimeters for electron and jet triggers. The second trigger stage, "Level 2", combines tracking data and clusters of energy in the calorimeters to form muon, electron, photon, and jet candidates. A list of calorimeter clusters is provided by a nearest-neighbor hardware cluster finder. For each cluster, the $\mathrm{E_T}$, average φ, and average η are determined. Jet candidates are selected from this list of clusters, and clusters that predominantly consist of electromagnetic calorimeter energy are identified as electron or photon candidates. A list of $r - \varphi$ tracks is provided by the central fast tracker (CFT) [8],

a hardware track processor, which uses fast timing information from the CTC as input. A list of muon stubs is obtained from the central muon detectors, and they are matched to CFT tracks to form muon candidates. CFT tracks can also be matched to electromagnetic energy clusters to form electron candidates. A decision by the Level 2 hardware to accept the event initiates full readout of the CDF detector data. The last trigger stage, "Level 3", performs full event reconstruction using software executed by commercial processors. Electron, muon, photon, and jet candidates are selected using algorithms similar to those employed in the final offline analysis, and a final trigger decision is made to output CDF data to magnetic tape.

CHAPTER 3

SELECTION OF PHOTON-LEPTON CANDIDATES

Photon-lepton candidates are obtained from three different samples of events selected by the Level 3 trigger: inclusive photon events and inclusive muon events, from which photon-muon candidates are selected; and inclusive electron events, from which photon-electron candidates are selected. The methods for lepton identification [9] and photon identification [10] are very similar to those of previous analyses. The offline identification requirements of photons and the selection of photon-muon candidates from the inclusive photon sample are described in Section 3.1; the offline identification requirements of muons and the selection of photon-muon candidates from a muon trigger sample are described in Section 3.2. The offline identification requirements of electrons and the selection of photon-electron candidates are described in Section 3.3. The identification requirements of missing transverse energy, additional photons, or additional leptons in the photon-lepton sample are described in Section 3.4. A description of the subsamples of photon-lepton candidates to be analyzed is given in Section 3.5.

All CDF data samples described in this paper are required to have: $|z_{event}|$ less than 60 cm, so that the collision is well-contained by the CDF detector; and no measurable energy in the calorimetry recorded out of time (more than 20 ns early or more than 35 ns late, as measured by TDC's within the CHA) with the $p\bar{p}$ collision time, in order to suppress cosmic ray events and backgrounds related to the Main Ring accelerator.

3.1 Photon Identification

Photon selection criteria are listed in Table 3.1 and are described below. For the energies considered here, the response of the CEM to photons is nearly identical to that of electrons; the reconstruction and identification of electrons and photons are therefore very similar, the chief difference being the high momentum track caused by the former and the absence of any tracks caused by the latter. Photon or electron candidates in the CEM are chosen from clusters of energy in adjacent CEM towers. A cluster starts from seed towers exceeding 3 GeV in energy, and spans three towers in η by one tower in φ, with no sharing of towers between different clusters. The total photon or electron energy is the sum of the energies of the towers in a cluster, where the energy scales of the CEM towers are calibrated by electrons from Z^0 decays. The energy resolution of a CEM electron or photon is given by [11]:

$$\begin{aligned}(\frac{\delta \mathrm{E}}{\mathrm{E}})^2 &= (\frac{(13.5 \pm 0.7)\%\ \mathrm{GeV}^{1/2}}{\sqrt{\mathrm{E_T}}})^2 \\ &\quad +(1.5 \pm 0.3\%)^2. \end{aligned} \tag{3.1}$$

The resolution for $\mathrm{E_T} > 25$ GeV is better than 3%.

For photons or electrons, the CES shower position is determined by the energy-weighted centroid of the highest energy clusters of those strips and wires in the CES corresponding to the seed tower of the CEM energy cluster; for electrons, the shower position is determined by the clusters of strips and wires in the CES closest to the position of the electron track, when the track is extrapolated to the CES radius. Similarly, the photon direction is determined by the line connecting the primary event vertex to the CES shower position, and the electron direction is determined by the electron track.

Photon Identification and Isolation Cuts		
CEM fiducial photon		
Photon E_T	$>$	25 GeV
Tracks with $p_T > 1$ GeV/c	$=$	0
Tracks with $p_T \leq 1$ GeV/c	$\leq$	1
HAD/EM	$<$	$0.055 + 0.00045$ GeV$^{-1} \times E^{\gamma}$
$\chi^2_{\rm Avg} = (\chi^2_{\rm Strip} + \chi^2_{\rm Wire})/2$	$<$	20
$E^{\rm CES}_{\rm 2nd}$	$<$	$2.39 + 0.01 \times E^{\gamma}$ GeV
E_T in a cone of 0.4, $E^{\rm Iso}_{\rm cone}$	$<$	2 GeV
p_T of tracks in a cone of 0.4	$<$	5 GeV/c

Table 3.1: The selection criteria used to identify photon candidates.

To ensure that events are well measured, the shower positions of electron or photon candidates are required to fall within the fiducial volume of the CEM. To be in the fiducial region, the shower position is required to lie within 21 cm of the tower center ($|X_{wire}| < 21.0$ cm) in the $r - \varphi$ view so that the shower is fully contained in the active region. The region $|\eta| < 0.05$, where the two halves of the detector meet, is excluded. The region $0.77 < \eta < 1.0, 75^\circ < \varphi < 90^\circ$ is uninstrumented because it is the penetration for the cryogenic connections to the solenoidal magnet. In addition, the region $1.0 < |\eta| < 1.1$ is excluded because of the smaller depth of the electromagnetic calorimeter in that region. The fiducial CEM coverage per photon or electron is 81% of the solid angle in the region defined by $|\eta| < 1.0$.

Photon candidates are required to have tracking and CEM shower characteristics consistent with that of a single, neutral, electromagnetically interacting particle. No CTC tracks with $p_T > 1$ GeV/c may point at the CEM towers in the photon cluster; at most one track with $p_T < 1$ GeV/c is allowed to point at these same towers. The ratio, HAD/EM, of the total energy of the CHA towers located behind the CEM towers in the photon cluster to the total energy of those CEM towers, is required to be less than $0.055 + 0.00045$ GeV$^{-1} \times E^{\gamma}$. A χ^2 test is used to compare the energy

Inclusive Photon Trigger		
CEM photon		
E_T	$>$	23 GeV
fiducial CES cluster		
$E^{Iso}_{3x3} < 4$ GeV OR $E_T > 50$ GeV		
Inclusive Electron Trigger		
CEM electron		
E_T	$>$	18 GeV
p_T	$>$	13 GeV/c
HAD/EM	$<$	0.125
χ^2 (CES strips)	$<$	10
Lshr	$<$	0.2
Track-CES matching:		
$\lvert\Delta x_{CES}\rvert$	$<$	3 cm
$\lvert\Delta z_{CES}\rvert$	$<$	5 cm
Inclusive Muon Trigger		
CMNP, CMUP, or CMX muon		
p_T	$>$	18 GeV/c
HAD energy	$<$	6 GeV
Track Stub Matching:		
$\lvert\Delta x_{stub}\rvert$	$<$	5 cm (CMNP, CMUP)
$\lvert\Delta x_{stub}\rvert$	$<$	10 cm (CMX)

Table 3.2: Level 3 trigger criteria for the inclusive photon, inclusive muon, and inclusive electron samples.

deposited in the CES wires (χ^2_{Wire}) and cathode strips (χ^2_{Strip}) to that expected from test beam data. The average of the two measurements, χ^2_{Avg}, is required to be less than 20. The CES cluster of second highest energy in the CEM seed tower, E^{CES}_{2nd}, is required to be less than $2.39 + 0.01 \times E^{\gamma}$ in units of GeV. The last two requirements ensure that the photon CEM cluster arises from a single photon and not from the two or more photons which are indicative of hadron decay.

Calorimeter and tracking data in a cone of $\eta - \varphi$ space, defined by a radius of $R = \sqrt{\Delta\eta^2 + \Delta\varphi^2} < 0.4$ surrounding the photon cluster, are used to discriminate photons produced in isolation from those originating in jets of hadrons. The total

transverse energy deposited in the calorimeters in a cone of $R = 0.4$ around the photon shower position is summed, and the photon E_T is subtracted. If there are multiple $p\bar{p}$ interactions in the event, the mean transverse energy in a cone of $R = 0.4$ per additional interaction, 0.23 GeV per interaction, is also subtracted. In addition, the mean transverse energy leakage of the photon shower into CEM towers outside the photon cluster, as a function of photon shower position, is also subtracted. The remaining energy in the cone is the photon isolation energy, E_{cone}^{Iso}, which is required to be less than 2 GeV. As an additional indicator of photon isolation, the sum of the momenta of CTC tracks incident upon a cone of $R = 0.4$ around the photon shower position must be less than 5 GeV.

An inclusive photon sample is selected with the CDF trigger requirements described below and summarized in Table 3.2. At Level 1, events are required to have at least one CEM trigger tower [12] with E_T exceeding 8 GeV. At Level 2, a low-threshold, isolated photon trigger selects events with CEM clusters exceeding 23 GeV in E_T (computed assuming $z_{event} = 0.0$). In addition, a CES energy cluster is required to accompany the CEM cluster, and the additional transverse energy deposited in an array of calorimeter towers spanning three towers in η by three towers in φ surrounding the CEM cluster, E_{3x3}^{Iso}, is required to be less than approximately 4 GeV. Alternatively at Level 2, a high-threshold photon trigger selects events with CEM clusters exceeding 50 GeV in E_T. At Level 3, the full offline CEM clustering is performed and events passing the low-threshold isolated photon trigger are required to have fiducial CEM clusters with $E_T > 23$ GeV; events passing the high-threshold photon trigger are required to have fiducial CEM clusters with $E_T > 50$ GeV. Events selected by these photon triggers are then required to have at least one photon candidate, satisfying all offline photon selection requirements,

with 25 GeV $<$ E_T $<$ 55 GeV for events passing the low-threshold trigger, or with E_T $\geq$ 55 GeV for events passing the high-threshold trigger. This results in an inclusive photon sample of 314,420 events. The measurement of the efficiency of the CDF trigger requirements of the inclusive photon sample, for events with at least one photon candidate, is described in Appendix A. The trigger efficiency for the low-threshold trigger increases from 43% to 89% as photon E_T increases from 25 GeV to 31 GeV, and remains constant at 89% from 31 GeV to 55 GeV. The trigger efficiency for the high-threshold trigger is greater than 99%. The detection efficiency of the offline photon selection criteria is $86.0 \pm 0.7\%$; the measurement is described in Appendix B.

Photon-muon candidate events are selected from the inclusive photon sample by requiring at least one muon in addition to the photon in the event. The muon can have any of the central muon stub types described in Section 3.2, the muon track must have $p_T > 25$ GeV/c, and all of the offline muon selection requirements must be satisfied, as described in Section 3.2 and summarized in Table 3.3. This results in a photon-muon sample of 28 events.

3.2 Muon Identification

Muons are identified by extrapolating CTC tracks through the calorimeters, and the extrapolation must match to a stub in either the CMU, CMP, or CMX. There are five different types of track-stub matches: tracks which intersect only the CMU and match a CMU stub (CMNP muons); tracks which intersect both the CMU and CMP and match stubs in both (CMUP muons); tracks which intersect both the CMU and CMP and match a stub in the CMU only (CMU muons); tracks which intersect the CMP and match a stub in the CMP only (CMP muons); and tracks

Electron candidates		
CEM fiducial electron		
Electron E_T	$>$	25 GeV
$p_T \times c$	$>$	$5/9 \times E_T$
Track-CES matching:		
$\lvert\Delta x_{CES}\rvert$	$<$	1.5 cm
$\lvert\Delta z_{CES}\rvert$	$<$	3 cm
Track-Vertex matching:		
$\lvert\Delta z_{event}\rvert$	$<$	5 cm
HAD/EM	$<$	0.05
χ^2 (CES strips)	$<$	10
$\lvert L_{shr}\rvert$	$<$	0.2
Photon conversion removal		
Isolation E_T	$<$	$0.1 \times E_T$
Muon candidates		
CMNP, CMUP, CMX, CMP, or CMU muon		
Track p_T	$>$	25 GeV/c
Track-Stub Matching:		
$\lvert\Delta x_{stub}\rvert$	$<$	5 cm (CMP, CMX)
$\lvert\Delta x_{stub}\rvert$	$<$	2 cm (all other)
Track-Vertex matching:		
$\lvert d_0\rvert$	$<$	0.3 cm
$\lvert\Delta z_{event}\rvert$	$<$	5 cm
CEM energy	$<$	2 GeV
CHA energy	$<$	6 GeV
CEM+CHA energy	$>$	0.1 GeV
Isolation E_T	$<$	$0.1c \times p_T$

Table 3.3: The selection criteria used to identify electron and muon candidates.

which intersect the CMX and match a stub in the CMX (CMX muons). For offline identification, CMP and CMX muons are required to have a matching distance less than 5 cm, and all other muon types are required to have a matching distance less than 2 cm. CTC tracks that are matched to muon stubs are required to be well-measured and to be consistent with originating from the primary event vertex. The muon track is required to have a minimum of six layers of CTC wire measurements, at least three of which must be axial wire measurements and at least 2 of which must

be stereo wire measurements. The distance of closest approach of the CTC track to the primary event vertex must be less than 3 mm in the $r-\varphi$ view (d_0), and less than 5 cm in the z direction (Δz_{event}). Muon tracks which match with z_{event} are refit with the additional constraint of originating from the primary event vertex ("beam-constrained"), which improves muon momentum resolution by a factor of approximately 2. The curvature resolution for beam-constrained muons satisfying all offline selection requirements is given by

$$\delta(1/\mathrm{p_T}) \quad = \quad (0.091 \pm 0.004) \times 10^{-2} (\mathrm{GeV/c})^{-1}, \tag{3.2}$$

corresponding to a $\mathrm{p_T}$ resolution of 2–8% for muons with $\mathrm{p_T}$ ranging from 25–100 GeV/c [11].

High energy muons are typically isolated, minimum-ionizing particles which have limited calorimeter activity. A muon traversing the CEM deposits an average energy of 0.3 GeV; muon candidates are therefore required to deposit less than 2 GeV total in the CEM tower(s) the muon track intersects. Similarly, muons traversing the CHA deposit an average energy of 2 GeV, and so muon candidates are required to deposit less than 6 GeV total in the intersecting CHA tower(s). An additional requirement that the sum of all energies in the intersecting CEM and CHA towers exceeds 0.1 GeV is imposed in order to suppress hadrons or cosmic rays which may have passed through cracks in the central calorimetry. Finally, in order to further suppress hadrons and muons arising from the decay of hadrons, the total transverse energy deposited in the calorimeters, in a cone of $R = 0.4$ around the muon track direction, must be less than 0.1 of the muon track $c\mathrm{p_T}$. The detection efficiency of the offline muon selection criteria is $93.0 \pm 0.3\%$; the measurement is described in Appendix B.

Photon-muon candidates are obtained from CDF muon triggers as follows. At Level 1, a muon stub is required in either the CMU or CMX. Muon p_T is inferred from the angle of incidence of the muon stub due to deflection by the magnetic field of the solenoid; CMU stub p_T must exceed 6 GeV/c, and CMX stub p_T must exceed 10 GeV/c. In addition, a minimum energy of 300 MeV is required in the CHA tower associated with the muon stub. At Level 2, a CFT track with $p_T > 12$ GeV/c is required to point within 5° of a CMUP, CMNP, or CMX muon stub triggered at Level 1. Level 2 inclusive muon triggers are prescaled due to bandwidth limitations; more restrictive (but not prescaled) triggers at Level 2 must be employed to increase the selection efficiency for photon-muon candidates. To this end, a Level 2 trigger without a prescale selects events which pass the Level 2 muon trigger requirements and which also have a calorimeter energy cluster with Level 2 cluster $E_T > 15$ GeV. At Level 3, as summarized in Table 3.2, a fully reconstructed CMUP, CMNP, or CMX muon is required, with maximum track-stub matching distances of 5 cm, 5 cm, and 10 cm, respectively. The muon track p_T must exceed 18 GeV/c, and the energy deposited in a CHA tower by the muon must be less than 6 GeV. Photon-muon candidates are selected from 313,963 events passing the Level 3 muon triggers by requiring at least one CMUP, CMNP, or CMX muon candidate satisfying all offline muon selection requirements, as described in Table 3.3, and at least one photon candidate satisfying all offline photon selection requirements, as described in Table 3.1. This results in a photon-muon sample of 20 events. When combined with the 28 photon-muon candidates from the photon triggers in Section 3.1, a sample of 29 unique photon-muon events is obtained. Of those 29 events, 9 events satisfied only the photon trigger requirements, 1 event satisfied only the muon trigger requirements, and 19 events satisfied both the photon and muon trigger requirements.

The measurement of the efficiency of the CDF muon trigger requirements for photon-muon candidates is described in Appendix A. The efficiency for CMUP photon-muon or CMNP photon-muon candidates is $84 \pm 3\%$; the efficiency for CMX photon-muon candidates is $68 \pm 5\%$. When photon-muon candidates from the muon triggers are combined with those from the photon triggers in Section 3.1, the combined trigger efficiency varies with photon E_T and muon stub type, with an average efficiency exceeding 90%.

3.3 Electron Identification

Electrons are identified in the CEM by matching high momentum CTC tracks to high energy CEM clusters, as summarized in Table 3.3. The track of highest p_T which intersects one of the towers in a CEM cluster is defined to be the electron track. An electron candidate is required to have the track p_T (in GeV/c) $>$ 5/9 of the CEM cluster E_T (in GeV). The track position, as extrapolated to the CES radius, is required to fall within 1.5 cm of the CES shower position of the cluster in the $r - \varphi$ view (Δx_{CES}), and within 3 cm of the CES shower position in the z direction (Δz_{CES}). The distance of closest approach of the CTC track to the primary event vertex must be less than 5 cm in the z direction (Δz_{event}).

The CEM shower characteristics of electron candidates must be consistent with that of a single charged particle. The ratio, HAD/EM, of the total energy of the CHA towers located behind the CEM towers in the electron cluster to that of the electron itself is required to be less than 0.05. A χ^2 test comparing the energy deposited in the CES cathode strips to that expected from test beam data is required to be less than 10. A comparison of the lateral shower profile in the CEM cluster with test beam data is parameterized by a dimensionless quantity, L_{shr}, which is required to have

a magnitude less than 0.2. Electrons from photon conversions are removed using an algorithm based on tracking information [9]. Finally, as an additional isolation requirement, the total transverse energy deposited in the calorimeters, in a cone of $R = 0.4$ around the electron track, must be less than 10% of the electron E_T. The detection efficiency of the offline electron selection criteria is $81.0 \pm 0.2\%$; the measurement is described in Appendix B.

Photon-electron candidates are obtained from a CDF electron trigger as follows. At Level 1, events are required to have at least one CEM trigger tower [12] with E_T exceeding 8 GeV. At Level 2, two CEM clusters with $E_T > 16$ GeV are required, with each cluster HAD/EM also required to be less than 0.125. The Level 3 electron trigger, summarized in Table 3.2, requires a CEM cluster with $E_T > 18$ GeV matched to a CTC track with $p_T > 13$ GeV/c. In addition, a set of electron identification criteria less selective than offline identification criteria is imposed: cluster HAD/EM is required to be less than 0.125; the CES cathode strip χ^2 is required to be less than 10; the magnitude of L_{shr} is required to be less than 0.2; and the electron track must match the CES position by 3 cm in Δx_{CES} and by 5 cm in Δz_{CES}.

Photon-electron candidates are selected from 474,912 events passing the Level 3 electron trigger by requiring at least one electron candidate satisfying all offline electron selection requirements, as described in Table 3.3, and at least one photon candidate satisfying all offline photon selection requirements, as described in Table 3.1. This results in a photon-electron sample of 48 events. The efficiency of the CDF electron trigger requirements for photon-electron candidates is $98.5 \pm 1.5\%$. The measurement of the trigger efficiency is described in Appendix A.

3.4 Selection of Additional Objects

In addition to inclusive photon-lepton production, this analysis investigates the associated production of other photons, other leptons, and large missing transverse energy. Identification of additional photon candidates is the same as that described in Section 3.1 and summarized in Table 3.1. The identification of additional leptons is less selective, because the presence of the primary photon and lepton provides good trigger efficiency and reduces the sources of misidentified particles.

The selection of additional electron candidates is identical to that of previous CDF analyses [13] and is summarized in Table 3.4. Additional electron candidates in the CEM ("LCEM electrons") are identified with criteria similar to, but looser than, that of the primary electron candidates in Section 3.3: electron E_T must be 20 GeV or greater; electron track p_T (in GeV/c) must exceed half of the electron E_T (in GeV); the HAD/EM ratio of the electron must be less than 0.1; and the total transverse energy deposited in the calorimeters, in a cone of $R = 0.4$ around the electron direction, must be less than 10% of the electron E_T. The detection efficiency of these electron selection criteria is $88.9 \pm 0.4\%$ for candidates with $E_T > 20$ GeV.

Additional electron identification is extended to the endplug and forward regions of the calorimeter. Electron candidates originate with clusters of energy in the PEM or FEM with cluster E_T in excess of 15 GeV and 10 GeV, respectively. For PEM electrons, a χ^2 test comparing the energy deposited in a 3×3 array of PEM towers surrounding the PEM cluster to that expected from test beam data, $\chi^2_{3\times3}$, is required to be less than 3. The ratio, HAD/EM, of the total energy of the PHA (FHA) towers located behind the PEM (FEM) towers in the electron cluster to that of the electron itself, is required to be less than 0.1. As an isolation requirement, the total transverse energy deposited in the calorimeters, in a cone of $R = 0.4$ around the

LCEM electron		
E_T	$>$	20 GeV
$p_T \times c$	$>$	$1/2 \times E_T$
HAD/EM	$<$	0.1
Isolation E_T	$<$	$0.1 \times E_T$
PEM electron		
E_T	$>$	15 GeV
HAD/EM	$<$	0.1
$\chi^2_{3\times3}$	$<$	3.0
Isolation E_T	$<$	$0.1 \times E_T$
FEM electron		
E_T	$>$	10 GeV
HAD/EM	$<$	0.1
Isolation E_T	$<$	$0.1 \times E_T$
CMI muon		
p_T	$>$	20 GeV/c
$\lvert\eta_\mu\rvert$	$<$	1.2
Track-Vertex matching:		
$\lvert d_0\rvert$	$<$	0.3 cm
$\lvert\Delta z_{event}\rvert$	$<$	5 cm
CEM energy	$<$	2 GeV
CHA energy	$<$	6 GeV
CEM+CHA energy	$>$	0.1 GeV
p_T of tracks in a cone of 0.4	$<$	$0.1 \times p_T$
Isolation E_T	$<$	$0.1c \times p_T$

Table 3.4: The selection criteria used to identify additional lepton candidates.

cluster direction, must be less than 10% of the cluster E_T. The detection efficiency of these selection criteria is $87.4 \pm 0.7\%$ for PEM electrons with $E_T > 15$ GeV and $75.4 \pm 2.6\%$ for FEM electrons with $E_T > 10$ GeV.

Additional muon candidates include: any muon satisfying the criteria in Table 3.3, with the muon p_T requirement lowered to 20 GeV/c; and isolated CTC tracks consistent with that of a minimum ionizing particle (CMI muons), the criteria for which are summarized in Table 3.4. CTC tracks in the central region of the detector ($|\eta_\mu| < 1.2$), which do not extrapolate to any of the central muon chambers, are required to have beam-constrained $p_T > 20$ GeV/c, and are required to satisfy all of the muon selection requirements in Section 3.2, with the following exceptions: the muon stub matching requirement is no longer employed; and the isolation requirements are supplemented by the requirement that the sum of the momenta of CTC tracks, incident upon a cone of $R = 0.4$ around the muon track, be less than 0.1 of the muon track p_T. The detection efficiency of these selection criteria is $91.3 \pm 1.3\%$ for CMI muons with $p_T > 20$ GeV/c.

The missing transverse energy of an event, $\not\!\!E_T$, is calculated as follows. For each tower of each calorimeter, a vector $\vec{E_T}^{\,i}$ is defined whose magnitude equals the calorimeter transverse energy, as determined by the line directed from the primary event vertex to the calorimeter tower center, and whose direction is that of the same line projected into the plane transverse to the beam direction. The opposite of the vector sum over all calorimeter towers,

$$\vec{\not\!\!E}_T(raw) = -\sum_i \vec{E_T}^{\,i}, \tag{3.3}$$

is a first approximation of $\not\!\!E_T$. In this paper, the measurement of $\not\!\!E_T$ is improved by the identification of jets, muons, electrons, and photons, as described below.

Jets of hadrons are identified via clusters of energy measured by the calorimeters. A jet reconstruction algorithm [14] finds clusters of energy deposited in cones of fixed radius $R = 0.4$. The jet energy and jet direction are measured using the total energy and the energy-weighted centroid, respectively, of the calorimeter towers contained in the cone. The jet energy is then corrected for non-linearity in the response of the calorimeters, the leakage of energy between calorimeter towers, the energy deposited outside of the jet cone, the energy from the underlying $p\bar{p}$ collision debris, and the energy from any additional $p\bar{p}$ interactions. These corrections result in mean increases of 70% (35%) to the raw jet $\mathrm{E_T}$, for jets with raw $\mathrm{E_T}$ of 10 GeV (100 GeV) [9].

An estimate of $\not\!\!\mathrm{E_T}$ which takes into account the corrected jet energies, $\not\!\!\mathrm{E_T}(j)$, is obtained from $\not\!\!\mathrm{E_T}(raw)$ by adding for each jet the raw jet momentum vector, $\vec{\mathrm{E}}^{j}_{\mathrm{T}\ raw}$, and subtracting the corrected jet momentum vector, $\vec{\mathrm{E}}^{j}_{\mathrm{T}\ cor}$:

$$\vec{\not\!\!\mathrm{E}}_{\mathrm{T}}(j) \;=\; \vec{\not\!\!\mathrm{E}}_{\mathrm{T}}(raw) - \sum_{j}(1 - \frac{\mathrm{E}^{j}_{\mathrm{T}\ raw}}{\mathrm{E}^{j}_{\mathrm{T}\ cor}})\vec{\mathrm{E}}^{j}_{\mathrm{T}\ cor}. \tag{3.4}$$

The jets included in this sum are required to have $\mathrm{E}^{j}_{\mathrm{T}\ raw} > 8$ GeV and $|\eta_j| < 2.4$.

Muons penetrate the calorimeters, so their energy is not accounted for in $\not\!\!\mathrm{E_T}(raw)$ and must be included separately. Muons with any combination of stubs in the central muon chambers are included in the $\not\!\!\mathrm{E_T}$ calculation, provided that: the beam-constrained muon track $\mathrm{p_T}$ exceeds 10 GeV/c; less than 6 GeV of energy is deposited in intersecting CHA towers; less than 2 GeV of energy is deposited in intersecting CEM towers; and Δx_{stub} satisfies the requirements in Table 3.3. High momentum tracks without matching muon chamber stubs are also included, provided that all of the CMI muon criteria in Table 3.4 are satisfied, except for the following differences:

the track need not extrapolate to regions uninstrumented by muon chambers; the isolation requirements in Table 3.4 are rescinded; and in their place is added the requirement that the total transverse energy deposited in the calorimeters, in a cone of $R = 0.4$ around the track direction, must be less than 5 GeV. An estimate of $\not\!\!E_{\rm T}$ which takes into account the muons described above, $\not\!\!E_{\rm T}(j\mu)$, is obtained from $\not\!\!E_{\rm T}(j)$ by subtracting for each muon the muon momentum vector, $\vec{\rm p}_{\rm T}^{\,\mu}$, and adding the transverse energy vector, $\vec{\rm E}_{\rm T}^{\,\mu}$, of the total energy deposited in intersecting CHA and CEM towers:

$$\vec{\not\!\!E}_{\rm T}(j\mu) \;=\; \vec{\not\!\!E}_{\rm T}(j) - \sum_{\mu}(1 - \frac{{\rm E}_{\rm T}^{\mu}}{c{\rm p}_{\rm T}^{\mu}})c\vec{\rm p}_{\rm T}^{\,\mu}. \tag{3.5}$$

The response of the calorimetry to high energy electrons and photons differs from that of jets of hadrons, so their energy is not properly accounted for by $\not\!\!E_{\rm T}(j\mu)$. The following types of electrons and photons are included in this correction: any CEM photon satisfying the criteria in Table 3.1; and any CEM, PEM, or FEM electron satisfying criteria identical to that listed in Table 3.4, except that the isolation requirements are rescinded. The final estimate of $\not\!\!E_{\rm T}$ which takes into account the electron and photon candidates described above, $\not\!\!E_{\rm T}(j\mu e\gamma)$, is obtained from $\not\!\!E_{\rm T}(j\mu)$ by subtracting for each electron or photon its transverse energy vector, $\vec{\rm E}_{\rm T}^{\,e,\gamma}$, and adding the transverse energy vector of the jet energy cluster corresponding to it, $\vec{\rm E}_{\rm T\ \mathit{cor}}^{\,j_{e,\gamma}}$:

$$\begin{aligned} \vec{\not\!\!E}_{\rm T} \;&\equiv\; \vec{\not\!\!E}_{\rm T}(j\mu e\gamma) \\ &=\; \vec{\not\!\!E}_{\rm T}(j\mu) - \sum_{e,\gamma}(\vec{\rm E}_{\rm T}^{\,e,\gamma} - \vec{\rm E}_{\rm T\ \mathit{cor}}^{\,j_{e,\gamma}}). \end{aligned} \tag{3.6}$$

3.5 Photon-Lepton Samples

The selection of 29 photon-muon events and 48 photon-electron events results in the "inclusive photon-lepton sample" of 77 events total. The purpose of this paper is to sort and analyze the inclusive and exclusive combinations of particles produced for events in this sample, the method for which is summarized in Figure 3.1.

The first step in understanding the sample composition is through the angular separation between the lepton and the photon. A two-particle final state is indicated by the identification of a single lepton and a single photon that are nearly opposite in azimuth. Since a two-particle photon-lepton final state would violate the conservation of lepton number, such events arise from the standard model in one of two ways: either the lepton or photon has been misidentified, or is associated with a jet of hadrons; or a second lepton which restores conservation of lepton number has evaded identification. The former is characterized by a photon and a lepton opposite in azimuth, while the latter is suppressed in this geometry, so such a sample isolates the majority of events with misidentified photons or leptons. To this end, the inclusive photon-lepton sample is analyzed as two subsamples: a "two-body photon-lepton sample" typical of a two-particle final state, and a "multi-body photon-lepton sample" typical of three or more particles in the final state. The selection requirements of the two-body photon-lepton sample are: exactly one photon and exactly one lepton satisfying the criteria summarized in Tables 3.1 and 3.3; no additional leptons satisfying the criteria in Table 3.4; and the nearest distance in azimuth between the photon and lepton, $\Delta\varphi_{\ell\gamma}$, must exceed 150°. The region $\Delta\varphi_{\ell\gamma} > 150°$ was chosen by requiring it to include 95% of Z^0 boson events decaying to two CEM electrons, which are a source of misidentified photons. Excluded from the two-body photon-lepton sample are those two-body photon-electron events

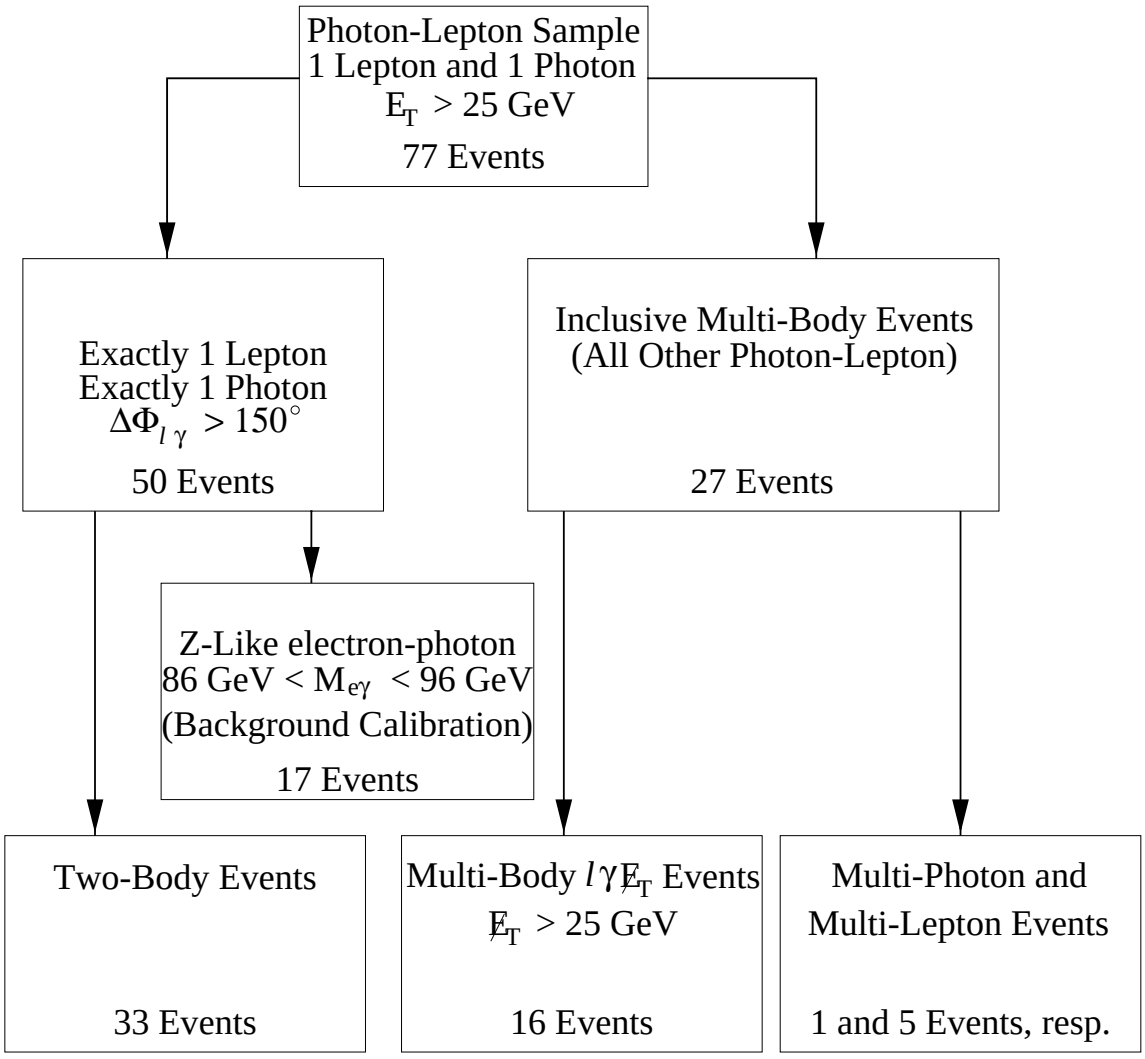

Figure 3.1: The subsets of inclusive photon-lepton events analyzed in this paper.

for which the photon-electron invariant mass, $M_{e\gamma}$, is within 5 GeV of M_Z. This "Z^0-like" control sample is used to estimate the photon misidentification rate from electrons, as described in Chapter 4.3. The multi-body sample is composed of the remaining inclusive photon-lepton events.

The multi-body sample is then further analyzed for the presence of large $\not\!\!E_T$, additional leptons, or additional photons. Multi-body events with $\not\!\!E_T > 25$ GeV, the "multi-body $\ell\gamma\not\!\!E_T$ sample", and multi-body events with one or more additional photons or leptons satisfying the criteria described in Section 3.4, the "multi-photon and multi-lepton sample", are studied concurrently with the two-body sample and the inclusive multi-body sample. The $\not\!\!E_T$ threshold of 25 GeV was chosen from previous analyses [15] as a significant indicator of a neutrino arising from leptonic decays of the W boson. Among these samples, the following properties are analyzed: the total event rate; the distribution of lepton E_T, photon E_T, and $\not\!\!E_T$; the distribution of the invariant mass of any relevant combinations of particles; and the angular distributions of any relevant combinations of particles.

CHAPTER 4

STANDARD MODEL SOURCES

4.1 $W\gamma$ and $Z^0\gamma$ Production

The dominant source of photon-lepton events at the Tevatron is electroweak diboson production, wherein an electroweak boson (W or Z^0) decays leptonically ($\ell\nu$ or $\ell\ell$) and a photon is radiated from either the initial state quark, a charged electroweak boson (W), or a charged final state lepton. The number of photon-lepton events from electroweak diboson production is estimated from a Monte Carlo event generator program written by Uli Baur and Stephen Mrenna [16]. The Baur-Mrenna program outputs 4-vectors of particles emanating from a diboson production event, and this output is used as input to a CDF detector simulation program, which outputs simulated data in a format identical to that of an actual CDF event. Simulated photon-lepton event rates can then be estimated in a manner identical to that of CDF data.

The Baur-Mrenna program is a set of leading-order matrix element calculations [17] which was incorporated into the PYTHIA [18] event generator program. The matrix element calculation for $W\gamma$ ($Z^0\gamma$) includes all tree-level diagrams with a $q\bar{q}'$ ($q\bar{q}$) initial state and a $\ell\nu_\ell\gamma$ ($\ell\ell\gamma$) final state, where ℓ is an e, μ, or τ, and the mediating electroweak boson is a real or virtual W (Z^0 or γ^*). Figure 4.1 shows the leading-order Feynman diagrams for $q\bar{q}' \to \ell\nu_\ell\gamma$. Figure 4.2 shows the leading-order Feynman diagrams for $q\bar{q} \to \ell\bar{\ell}\gamma$.

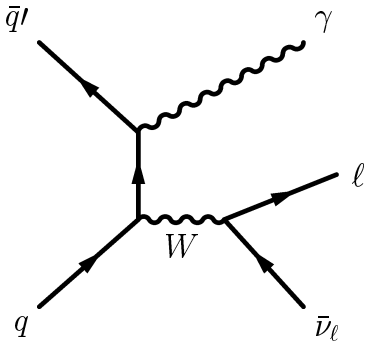

a) Initial state photon radiation

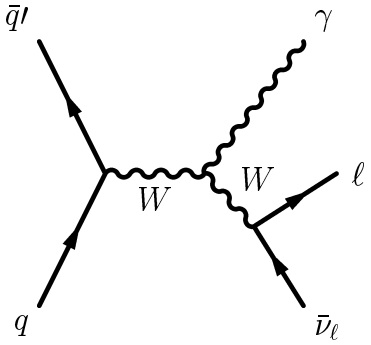

b) W final state photon radiation

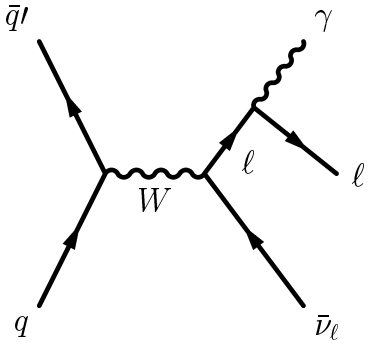

c) Lepton final state photon radiation

Figure 4.1: The leading-order Feynman diagrams for photon radiation in the process $q\bar{q}\prime \to \ell\bar{\nu}_\ell\gamma$.

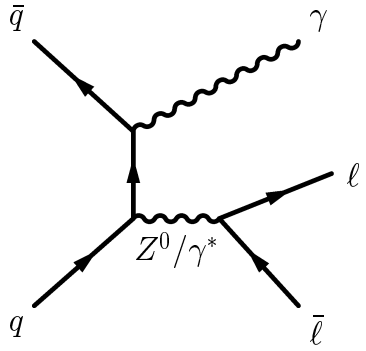

a) Initial state photon radiation

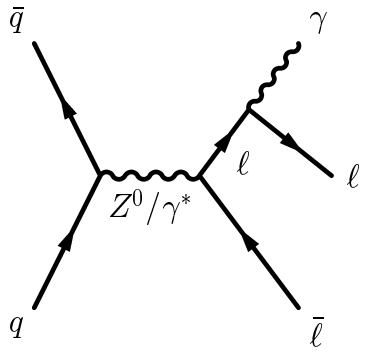

b) Lepton final state photon radiation

Figure 4.2: The leading-order Feynman diagrams for photon radiation in the process $q\bar{q} \to \ell\bar{\ell}\gamma$.

The region of phase space where the final state lepton and photon are collinear is carefully sampled, taking into account the lepton mass for each lepton flavor. This allows reliable calculations to be made for all photon-lepton separation angles and for photon E_T well below (< 1 GeV) those considered in this analysis. PYTHIA generates, fragments, and hadronizes the partons described by the matrix elements. The leading-order proton structure function CTEQ5L [19] is used to compute the matrix elements. The TAUOLA [20] program is used to compute the decays of τ leptons. Each generated event is assigned a weight proportional to the probability of its occurrence as determined by the matrix element calculation.

Generated events are used as input to a program which simulates the CDF detector response to the final state particles. The simulation includes the following features relevant to this analysis: the z_{event} distribution of $p\bar{p}$ collisions observed in CDF data; the geometric acceptance of all CDF detector subsystems; charged particle tracking in the CTC; the tower-by-tower response of the calorimetry to final state particles; the CES response to electromagnetic showers; and the response of the central muon chambers to penetrating charged particles. The program is not used to simulate the CDF trigger, the z_{event} distribution beyond $|z_{event}| = 60$ cm, nor the energy-out-of-time distribution; the event selection efficiencies for these must be applied as separate corrections to the simulated event rates. There also exist 6-8% differences between the lepton (and photon) detection efficiencies found in CDF data and the efficiencies similarly computed in simulated data, as described in Chapter 3. Simulated event rates containing particles of type X are therefore adjusted by a ratio C_X of detection efficiencies in CDF data to that of simulated events,

$$C_X = \epsilon^{data}_{XID}/\epsilon^{sim}_{XID}, \tag{4.1}$$

Particle	ϵ_{XID}^{data}	ϵ_{XID}^{sim}	C_{XID}
CEM photon	0.86	0.93	0.93 ± 0.04
CEM electron	0.81	0.88	0.92 ± 0.04
2nd CEM electron	0.89	0.97	0.91 ± 0.05
PEM electron	0.92	0.99	0.94 ± 0.03
FEM electron	0.75	0.98	0.77 ± 0.12
central muon	0.93	0.99	0.94 ± 0.03
CMI muon	0.91	0.99	0.92 ± 0.04

Table 4.1: Corrections to the simulated particle identification efficiencies obtained from CDF data. Included are the efficiencies measured directly from CDF data (ϵ_{XID}^{data}), the efficiencies measured from simulated data (ϵ_{XID}^{sim}), and the corrections to simulated rates (C_{XID}).

where ϵ_{XID}^{data} is the detection efficiency of X in CDF data and ϵ_{XID}^{sim} is the corresponding efficiency in simulated data. The systematic uncertainty is estimated to be half of the difference between C_X and unity. Table 4.1 lists the corrections for the various types of leptons and photons analyzed. The measurement of the detection efficiencies is discussed in Appendix B.

Simulated events with PEM electrons are an exception to this procedure, since the PEM shower shape quantity $\chi^2_{3\times3}$ is not included in the detector simulation. The PEM electron detection efficiency for all the requirements in Table 3.4, except the $\chi^2_{3\times3}$ requirement, is measured and corrected for as other leptons are; the correction is listed in Table 4.1. The efficiency of the $\chi^2_{3\times3}$ requirement for PEM electrons which satisfy all other requirements, $\epsilon_{PEM}^{\chi^2}$, is then measured separately using CDF data to be $95.0 \pm 0.5\%$, as described in Appendix B. This comprises an additional correction to the identification efficiency for simulated events with PEM electrons.

Item	Value	Relative Uncertainty
K_{NLO}	1.30 ± 0.10	7.7%
σ_{LO}	105.0 ± 5.3 pb	5.0%
$\sum w_{pass} / \sum w_{tot}$	$(2.57 \pm 0.12) \times 10^{-4}$	4.7%
ϵ_{trig}	0.985 ± 0.015	1.5%
C_{sim}	0.792 ± 0.052	6.6%
$\int Ldt$	86.34 ± 3.52 pb^{-1}	4.1%
$\bar{N}_{e\gamma}$	2.36 ± 0.31	13.1%

Table 4.2: The mean number of multi-body photon-electron events, $\bar{N}_{e\gamma}$, expected from $W(\rightarrow e\nu) + \gamma$. The factors used in Equation 4.2 and their uncertainties are also shown.

The mean contribution to photon-lepton candidates in CDF data, $\bar{N}_{\ell\gamma}$, for a particular generated process is given by

$$\begin{aligned} \bar{N}_{\ell\gamma} &= \sigma_{LO} \times K_{NLO} \times \epsilon_{trig} \times C_{sim} \times \int Ldt \\ &\quad \times (\sum w_{pass})/(\sum w_{tot}), \end{aligned} \tag{4.2}$$

where

- σ_{LO} is the leading order cross section computed by the event generator for a given process with a given set of generator-level cuts and thresholds. The uncertainty due to generator statistics is negligible. The uncertainty due to PDF normalization is taken to be $\pm 5\%$, as recommended in [21].

- K_{NLO} is the next-to-leading order (NLO) QCD K-factor for $W\gamma$ ($Z^0\gamma$) production estimated from NLO calculations [22]. The K-factors used are 1.30 ± 0.10 for $W\gamma$ production and 1.25 ± 0.05 for $Z^0\gamma$ production, where the uncertainties are estimated from the QCD renormalization scale dependence of the NLO cross section.

- ϵ_{trig} is the trigger efficiency for photon-lepton events described in Appendix A. It is applied to events of the appropriate photon E_T and lepton type through a simple trigger simulation which emulates the results in Table A.2. For photon-electron events $\epsilon_{trig} = 98.5 \pm 1.5\%$; for photon-muon events ϵ_{trig} varies with muon type and photon E_T, with an average efficiency of 94% for simulated $W\gamma$ events satisfying all selection criteria. The uncertainty of the photon-muon trigger efficiency is $\pm 6\%$.

- C_{sim} is the product of the correction factors to the detection efficiencies computed by the CDF detector simulation:

  C_{z60}, the efficiency for the requirement $|z_{event}| < 60$ cm, measured to be 0.95 ± 0.02;

  C_{EOT}, the efficiency for the requirement E_T(out-of-time) $= 0$, measured to be 0.975 ± 0.004 [23];

  the product over the leptons and photons identified by the detector simulation, $\prod_{i=1}^{n} C_{X_i ID}$, of corrections $C_{X_i ID}$ to the simulated particle identification efficiencies listed in Table 4.1;

  and $\epsilon^{\chi^2}_{PEM}$, an additional correction factor for each PEM electron identified by the detector simulation, measured to be 0.953 ± 0.005 and described above.

- $\int Ldt$ is the integrated luminosity for the 1994-5 run employed in this analysis, 86.34 ± 3.52 pb^{-1} [24].

- $\sum w_{pass}$ is the sum of the weights of the simulated events satisfying all selection criteria. The uncertainty is given by $\sqrt{\sum w^2_{pass}}$, which is typically a few percent.

	Two-Body Events	
Process	$e\gamma X$	$\mu\gamma X$
$\gamma + W$ production		
$\gamma + W \to \ell\nu$	1.09 ± 0.14	1.44 ± 0.19
$\gamma + W \to \tau\nu$	0.08 ± 0.02	0.09 ± 0.02
Subtotal	1.17 ± 0.15	1.52 ± 0.21
$\gamma + Z^0$ production		
$\gamma + Z^0 \to \ell\ell$	5.06 ± 0.54	6.53 ± 0.76
$\gamma + Z^0 \to \tau\tau$	0.34 ± 0.05	0.53 ± 0.08
Subtotal	5.40 ± 0.57	7.06 ± 0.82
Total	6.57 ± 0.68	8.58 ± 0.97

Table 4.3: The estimated $W\gamma$ and $Z^0\gamma$ backgrounds for two-body photon-lepton events. There exist correlated uncertainties between the different photon-lepton sources.

- $\sum w_{tot}$ is the sum of the weights of all simulated events, with uncertainty given by $\sqrt{\sum w_{tot}^2}$, which is typically negligible.

Table 4.2 shows a sample calculation for multi-body photon-electron events originating from $W(\to e\nu)+\gamma$ production. The uncertainty in the mean rate has roughly equal contributions from the NLO K-factor, simulation systematics, luminosity, proton structure, and generator statistics. Other simulated processes have similar uncertainties.

Table 4.3 shows the results of all simulated processes, for inclusive two-body events; Table 4.4 shows the same results for inclusive multi-body events and multi-body $\ell\gamma\not\!\!E_{\rm T}$ events. The slightly larger contribution of two-body $\mu\gamma$ events relative to $e\gamma$ events is due to the explicit exclusion of $e\gamma$ events whose invariant mass is "Z^0-like" (86 GeV $< M_{e\gamma} <$ 96 GeV). There are no significant differences between the inclusive multi-body rates for $e\gamma$ and $\mu\gamma$ production. In the case of $Z^0\gamma$ production, there is a larger number of multi-body $\mu\gamma\not\!\!E_{\rm T}$ events (1.0) relative to $e\gamma\not\!\!E_{\rm T}$ events (0.3). The difference is due to events where the second muon falls outside the solid

	Multi-Body Events			
Process	$e\gamma X$	$\mu\gamma X$	$e\gamma \not\!\!E_{\rm T}$	$\mu\gamma \not\!\!E_{\rm T}$
$\gamma + W$ production				
$\gamma + W \to \ell\nu$	2.36 ± 0.31	2.47 ± 0.33	1.89 ± 0.25	1.94 ± 0.26
$\gamma + W \to \tau\nu$	0.08 ± 0.02	0.06 ± 0.01	0.04 ± 0.01	0.05 ± 0.01
Subtotal	2.44 ± 0.32	2.53 ± 0.34	1.93 ± 0.26	1.99 ± 0.27
$\gamma + Z^0$ production				
$\gamma + Z^0 \to \ell\ell$	4.88 ± 0.53	4.49 ± 0.53	0.28 ± 0.05	0.90 ± 0.14
$\gamma + Z^0 \to \tau\tau$	0.13 ± 0.03	0.11 ± 0.02	0.03 ± 0.01	0.05 ± 0.01
Subtotal	5.01 ± 0.54	4.60 ± 0.54	0.32 ± 0.05	0.96 ± 0.15
Total	7.45 ± 0.78	7.13 ± 0.82	2.25 ± 0.28	2.95 ± 0.37

Table 4.4: The estimated $W\gamma$ and $Z^0\gamma$ backgrounds for inclusive multi-body photon-lepton events and multi-body $\ell\gamma \not\!\!E_{\rm T}$ events. There exist correlated uncertainties between the different photon-lepton sources.

angle in which muons can be detected ($|\eta_\mu| > 1.2$), subsequently inducing missing $\rm E_T$ equal to the $\rm p_T$ of the second muon. Leptons from τ decays contribute to the total photon-lepton rate at a level far below the leptonic branching ratio of a τ (about 3% accepted compared to a leptonic branching ratio of 18%) because the average lepton $\rm E_T$ is much lower than that of leptons from the direct decay of a W or Z^0.

Tables 4.5 and 4.6 shows the results of all simulated processes for multi-body photon-lepton events with additional leptons or photons, respectively. More $ee\gamma$ events than $\mu\mu\gamma$ events are expected due to the larger detector acceptance for additional electrons, which are identified in the central, plug, and forward calorimeters.

4.2 Jets Misidentified as Photons

A jet of hadrons initiated by a final state quark or gluon can contain mesons which decay to photons, such as the π^0, η, or ω. If one or more of these photons constitute a sufficiently large fraction of the jet momentum, then the hadron jet can be

	Multi-Body Events		
Process	$ee\gamma$	$\mu\mu\gamma$	$e\mu\gamma$
$\gamma + W$ production			
$\gamma + W \to \ell\nu$	—	—	—
$\gamma + W \to \tau\nu$	—	—	—
Subtotal	—	—	—
$\gamma + Z^0$ production			
$\gamma + Z^0 \to \ell\ell$	3.25 ± 0.44	2.19 ± 0.30	—
$\gamma + Z^0 \to \tau\tau$	—	—	0.05 ± 0.01
Subtotal	3.25 ± 0.44	2.19 ± 0.30	0.05 ± 0.01
Total	3.25 ± 0.44	2.19 ± 0.30	0.05 ± 0.01

Table 4.5: The estimated $W\gamma$ and $Z^0\gamma$ backgrounds for multi-body photon-lepton events with additional leptons. There exist correlated uncertainties between the different photon-lepton sources. The expected contributions from $W\gamma$ production are negligible.

misidentified by the CDF detector as a single prompt photon. Such a jet produced in association with a lepton candidate contributes to the detected photon-lepton candidates.

The contribution of lepton plus misidentified jet events is determined by counting the number of jets in CDF lepton data, $N_{\ell jet}$, and then multiplying that number by an estimate of the probability of a jet being misidentified as a photon, P_γ^{jet}, to obtain the number of photon-lepton candidates,

$$N_{\ell\gamma} = N_{\ell jet} \times P_\gamma^{jet}. \tag{4.3}$$

Lepton-jet candidates are selected from inclusive electron and muon triggers as follows. The Level 1 trigger and Level 3 trigger requirements are identical to those enumerated in Sections 3.2 and 3.3 of Chapter 3. The Level 2 trigger requirements differ from those of the photon-lepton sample due to the absence of the photon. Electron-jet events must be accepted by a Level 2 electron trigger, which requires

	Multi-Body Events	
Process	$e\gamma\gamma$	$\mu\gamma\gamma$
$\gamma + W$ production		
$\gamma + W \to \ell\nu$	—	—
$\gamma + W \to \tau\nu$	—	—
Subtotal	—	—
$\gamma + Z^0$ production		
$\gamma + Z^0 \to \ell\ell$	0.012 ± 0.012	0.004 ± 0.004
$\gamma + Z^0 \to \tau\tau$	—	—
Subtotal	0.012 ± 0.012	0.004 ± 0.004
Total	0.012 ± 0.012	0.004 ± 0.004

Table 4.6: The estimated $W\gamma$ and $Z^0\gamma$ backgrounds for multi-body photon-lepton events with additional photons. There exist correlated uncertainties between the different photon-lepton sources. The expected contributions from $W\gamma$ production are negligible.

a CEM energy cluster with $E_T > 16$ GeV; a cluster HAD/EM < 0.125; and a CFT track matching the CEM cluster with $p_T > 12$ GeV/c. The efficiency of these electron trigger requirements has been measured to be $\epsilon_e = 90.9 \pm 0.3\%$ [25]. Muon-jet events are selected from the Level 2 inclusive muon triggers described in Chapter 3.2, which have the same efficiency as the muon triggers described in Appendix A, except that they are prescaled due to bandwidth limitations. The prescaling results in a reduction of the trigger efficiency by a factor of 0.43 ± 0.02 for CMX muons, 0.43 ± 0.02 for CMNP muons, and 1.0 (no prescale) for CMUP muons. Requiring a Level 2 muon trigger precludes the use of CMP or CMU muons.

The requirements for lepton-jet candidates are: one or more lepton candidates satisfying the criteria in Table 3.3; and one or more jets with $|\eta_j| < 1.0$, jet $E_T > 25$ GeV, and a separation distance of the jet from the lepton in $\eta - \varphi$ space, $\Delta R_{\ell j}$, greater than 0.5. As a further step to prevent electrons from Z^0 boson decays being counted as jets, jet candidates must have electron-jet separation $\Delta R_{ej} > 0.5$

for all central electrons satisfying the selection criteria for additional electrons listed in Table 3.4. Table 4.8 shows the raw total number of jets, summed over all lepton-jet candidate events, for the various signal regions of this analysis.

Because the lepton trigger requirements of the lepton-jet sample are less efficient than the trigger requirements of the photon-lepton sample, the effective number of jets which potentially contribute to the photon-lepton candidates must be augmented by a ratio of the efficiencies of the different trigger paths. For electron-jet events with exactly one electron, this is simply a constant, $\epsilon_{e\gamma}/\epsilon_e = 1.08 \pm 0.02$; for muon-jet events with exactly one muon, the efficiency ratio, $R_{\mu_i\gamma}$, varies with muon stub type and jet $\mathrm{E_T}$,

$$R_{\mu_i\gamma} = \frac{\epsilon_{\mu_i} + (1 - \epsilon_{\mu_i}) \times \epsilon_\gamma(\mathrm{E_T})}{P_{\mu_i}\epsilon_{\mu_i}} \tag{4.4}$$

where ϵ_{μ_i} is the trigger efficiency for muons of stub type i, P_{μ_i} is the inclusive muon trigger prescale for muons of stub type i, and $\epsilon_\gamma(\mathrm{E_T})$ is the trigger efficiency of the photon candidate a jet would produce in the event of jet misidentification, as a function of photon $\mathrm{E_T}$. This ratio is evaluated for each jet in each event, and the sum over all jets in all events gives the total effective number of jets. Because CMU and CMP muons have been excluded from the lepton-jet sample, the number of jets in muon-jet events must be additionally multiplied by a factor of 1.14 ± 0.03 to compensate for the acceptance lost relative to that of photon-lepton events. This lost acceptance was calculated from the $W\gamma$ and $Z\gamma$ simulation described in Chapter 4.1.

For lepton-jet events with multiple leptons, the presence of the additional lepton increases the efficiency of the lepton trigger requirements, and the efficiency ratio of such events relative to the corresponding photon-lepton events must be accounted for separately. For electron-jet events with an additional CEM electron, the trigger

efficiency for both electron-jet and photon-electron events is nearly 100%, so that the trigger efficiency ratio of such events is assumed to be unity. Electron-jet events with additional PEM or FEM electrons have the same efficiency ratio as that of single electron-jet events above. For muon-jet events with an additional CMNP, CMUP, or CMX muon, the trigger efficiency ratio depends upon the muon trigger efficiencies of the two muon stub types:

$$R_{\mu_i\mu_j\gamma} = \frac{\epsilon_{\mu_i\mu_j} + (1 - \epsilon_{\mu_i\mu_j}) \times \epsilon_\gamma(\mathrm{E_T})}{P_{\mu_i}\epsilon_{\mu_i} + (1 - P_{\mu_i}\epsilon_{\mu_i}) \times P_{\mu_j}\epsilon_{\mu_j}}, \tag{4.5}$$

where ϵ_{μ_i} and ϵ_{μ_j} are the muon trigger efficiencies of the two different muon stub types, P_{μ_i} and P_{μ_j} are the inclusive muon trigger prescales of the two different muon stub types, and $\epsilon_{\mu_i\mu_j}$ is the efficiency of the logical OR of the two muon triggers,

$$\epsilon_{\mu_i\mu_j} \equiv \epsilon_{\mu_i} + (1 - \epsilon_{\mu_i}) \times \epsilon_{\mu_j}. \tag{4.6}$$

Muon-jet events with additional CMU, CMP, or CMI muons have the same efficiency ratio as that of single muon-jet events above.

The total effective number of jets in lepton-jet candidate events after all corrections have been applied is also given in Table 4.8. For two-body lepton-jet and inclusive multi-body lepton-jet events, there are more electron-jet candidates than muon-jet candidates because of the presence of non-electroweak sources of electron candidates (heavy flavor decay, photon conversion, stable hadrons misidentified as electrons, etc.). This is borne out by an increased electron-muon discrepancy for two-body events versus multi-body events, as expected from QCD dijet production. For multi-body lepton-jet events with $\not\!\!\mathrm{E_T} > 25$ GeV, electron-jet and muon-jet candidates are roughly equal, as would be expected from W-jet production. Comparing

Table 4.8 with Tables 4.3–4.6, it is concluded that in order to measure photon-lepton processes with electroweak-sized cross sections and a signal-to-background ratio greater than 1:1, P_{γ}^{jet} must be less than approximately 10^{-3}.

Mesons which decay to photons are typically only a portion of a shower of hadrons initiated by a high $\mathrm{E_T}$ quark or gluon. Other hadrons in the shower will deposit energy in the calorimeter close to the electromagnetic shower produced by these photons. Prompt photons (or electrons, which shower similarly) produced in the hard scattering of partons do not exhibit additional nearby calorimetric energy, therefore the additional $\mathrm{E_T}$ measured in a cone of $R = 0.4$ around the electromagnetic shower position, $\mathrm{E_{cone}^{Iso}}$, serves as a discriminant between prompt photons and misidentified jets. This discriminant is already employed in the photon selection (Table 3.1), by requiring $\mathrm{E_{cone}^{Iso}} < 2$ GeV. If the distribution of $\mathrm{E_{cone}^{Iso}}$ is relatively flat for misidentified jets, the distribution of $\mathrm{E_{cone}^{Iso}}$ of the photon candidates which fail this requirement can be extrapolated linearly to estimate the number of misidentified jets which satisfy it.

The probability that a jet is misidentified as a photon is determined from samples of jets and photons in events with a lepton trigger. Lepton candidates in lepton-triggered jet events are selected with the same trigger requirements as the lepton-jet sample described above. Instead of applying the full lepton selection criteria in Table 3.3, the minimal set of Level 3 lepton trigger requirements, listed in Table 3.2, is applied in this selection, so as to maximize the sample size. Along with exactly one such loose lepton candidate, lepton-triggered jet events are required to have exactly one jet with $|\eta_j| < 1.0$, $\mathrm{E_T} > 25$ GeV, and $\Delta R_{\ell j} > 0.5$. The lepton-triggered jet sample consists of 46091 electron-triggered jet events and 12875 muon-triggered jet events.

Lepton candidates in lepton-triggered photon events are selected with the same trigger requirements as the lepton-triggered jet events described above, except that the prescaled Level 2 inclusive muon trigger requirements are replaced by the muon-jet trigger described in Chapter 3.2. Lepton-triggered photon events are required to have exactly one loose lepton candidate as above, and are required to have exactly one photon candidate satisfying all of the photon selection criteria in Table 3.1, except for the isolation requirements. Specifically, the requirement that the sum of the p_T of all tracks in a cone of $R = 0.4$ around the photon be less than 5 GeV/c is rescinded, and the E_{cone}^{Iso} requirement is loosened from 2 GeV to 12 GeV. The lepton-triggered photon sample consists of 121 photon-electron and 38 photon-muon events.

Since the muon-triggered jet sample has a less efficient trigger path than the muon-triggered photon sample, an unbiased comparison of the two samples requires that the number of muon-triggered jet events must be augmented by the ratio of trigger efficiencies, in this case equal to the inverse of the efficiency of the Level 2 inclusive muon trigger prescale for each muon stub type, $1/P_{\mu_i}$, on an event-by-event basis. This increases the effective number of muon-triggered jet events from 12875 to 17745.

Photon candidates in the lepton-triggered photon sample consist of a combination of prompt photons, electrons misidentified as photons, and jets misidentified as photons, where only the jet component is relevant to the evaluation of P_γ^{jet}. The distribution of E_{cone}^{Iso} of the other two components is measured using a sample of CEM electrons from Z^0 decays. Dielectron events are selected from events satisfying the same trigger criteria as that of the photon-electron candidates described in Chapter 3.3. From these triggers a sample of Z^0-like dielectron events is selected which

has exactly two CEM electrons passing the electron criteria in Table 3.3, excepting the isolation requirement (that the total E_T deposited in the calorimeters, in a cone of $R = 0.4$ around the electron track, be less than 10% of the electron E_T), and requiring dielectron invariant mass within 5 GeV of M_Z. The distribution of E_{cone}^{Iso} normalized to unity, dN_Z/dE_{cone}^{Iso}, for the 3300 electrons in this sample is shown in Figure 4.3. CEM electron showers—which have the same calorimeter response as CEM showers from prompt photons—exhibit $E_{cone}^{Iso} < 2$ GeV 95% of the time.

Using the measured distribution dN_Z/dE_{cone}^{Iso} for prompt photons or electrons, and assuming a linear distribution in E_{cone}^{Iso} for jets misidentified as photons, the total number of photon candidates as a function of E_{cone}^{Iso}, dN/dE_{cone}^{Iso}, is given by

$$\frac{dN}{dE_{cone}^{Iso}} = A_1 \times \frac{dN_Z}{dE_{cone}^{Iso}} + A_2 \times E_{cone}^{Iso} + A_3, \tag{4.7}$$

where A_1, A_2, and A_3 are free parameters to be fit to the data. If the bin size is chosen to be equal to the E_{cone}^{Iso} threshold for isolated photon candidates (2 GeV), then A_1 is simply the number of prompt photon (or electron misidentified as photon) candidates with $E_{cone}^{Iso} < 2$ GeV, and $A_3 - A_2$ is the number of jets misidentified as photons with $E_{cone}^{Iso} < 2$ GeV. If in addition the normalization of the distribution is chosen to be the ratio of the number of lepton-triggered photon events (121 photon-electron and 38 photon-muon) to that of the effective number of lepton-triggered jet events (46091 electron-jet and 17745 muon-jet), then $A_3 - A_2$ is identically the jet misidentification rate P_γ^{jet}.

Employing these conventions, the distribution dN/dE_{cone}^{Iso} for lepton-triggered photon events is shown in Figure 4.4. The distribution (solid points) is peaked in the first bin corresponding to isolated photon candidates, followed by a linearly falling tail of non-isolated photon candidates. The minimum χ^2 fit of the data to

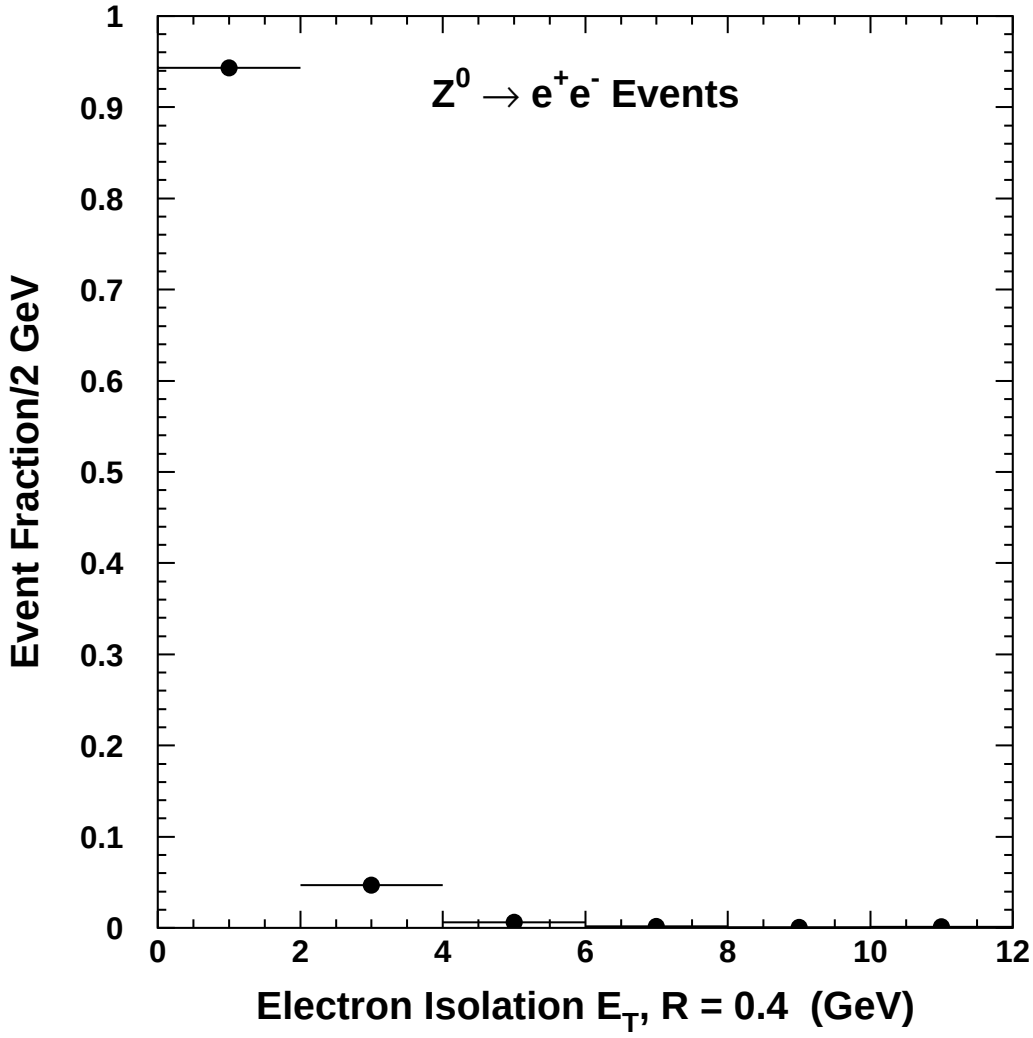

Figure 4.3: The distribution of E_{cone}^{Iso} for CEM electrons from Z^0 decays, normalized to unity.

	Lepton-Jet Samples		
	ej	μj	ℓj
photons	121	38	159
jets	46091	17745	63836
$A_1(10^{-4})$	13 ± 2	14 ± 4	13 ± 2
$A_2(10^{-4})$	-0.4 ± 0.1	-0.2 ± 0.2	-0.4 ± 0.1
$A_3(10^{-4})$	4.7 ± 0.9	2.4 ± 1.5	4.2 ± 0.7
χ^2/d.o.f.	0.38	0.44	0.42
$P_\gamma^{jet}(10^{-4})$	4.3 ± 1.0	2.2 ± 1.5	3.8 ± 0.7

Table 4.7: The results of fitting $dN/d\mathrm{E}_{\mathrm{cone}}^{\mathrm{Iso}}$ to photon candidates in CDF jet data obtained with a lepton trigger. Included are the number of photons and jets in each sample, the best fit parameters A_i, the χ^2 per degree of freedom for the fit, and the jet misidentification rate P_γ^{jet}.

the functional form of Equation 4.7 (solid line) is shown in Figure 4.4, along with the linear portion of the fit obtained from A_2 and A_3 (dashed line). The functional form chosen describes the data well (χ^2/d.o.f. $= 0.38$), yielding an average jet misidentification rate P_γ^{jet} of $3.8 \pm 0.7 \times 10^{-4}$. The best fit parameters are shown in Table 4.7.

Also shown in Figure 4.4 is an estimate of $dN/d\mathrm{E}_{\mathrm{cone}}^{\mathrm{Iso}}$ obtained from a simulation of W-jet production (cross-hatched histogram), using the PYTHIA event generator and the detector simulation described in Chapter 4.1. The leading-order Feynman diagrams for W-jet production employed by the PYTHIA event generator are shown in Figure 4.5. Simulated events are selected which satisfy the same requirements as the lepton-triggered jet and lepton-triggered photon samples obtained from the data, and photon candidates are required to arise solely from hadron decay. The simulated results for $dN/d\mathrm{E}_{\mathrm{cone}}^{\mathrm{Iso}}$ exhibit a shape consistent with a linear functional form, as well as a magnitude consistent with the observed jet misidentification rate.

Figure 4.6 shows the distribution $dN/d\mathrm{E}_{\mathrm{cone}}^{\mathrm{Iso}}$ computed for electron-triggered pho-

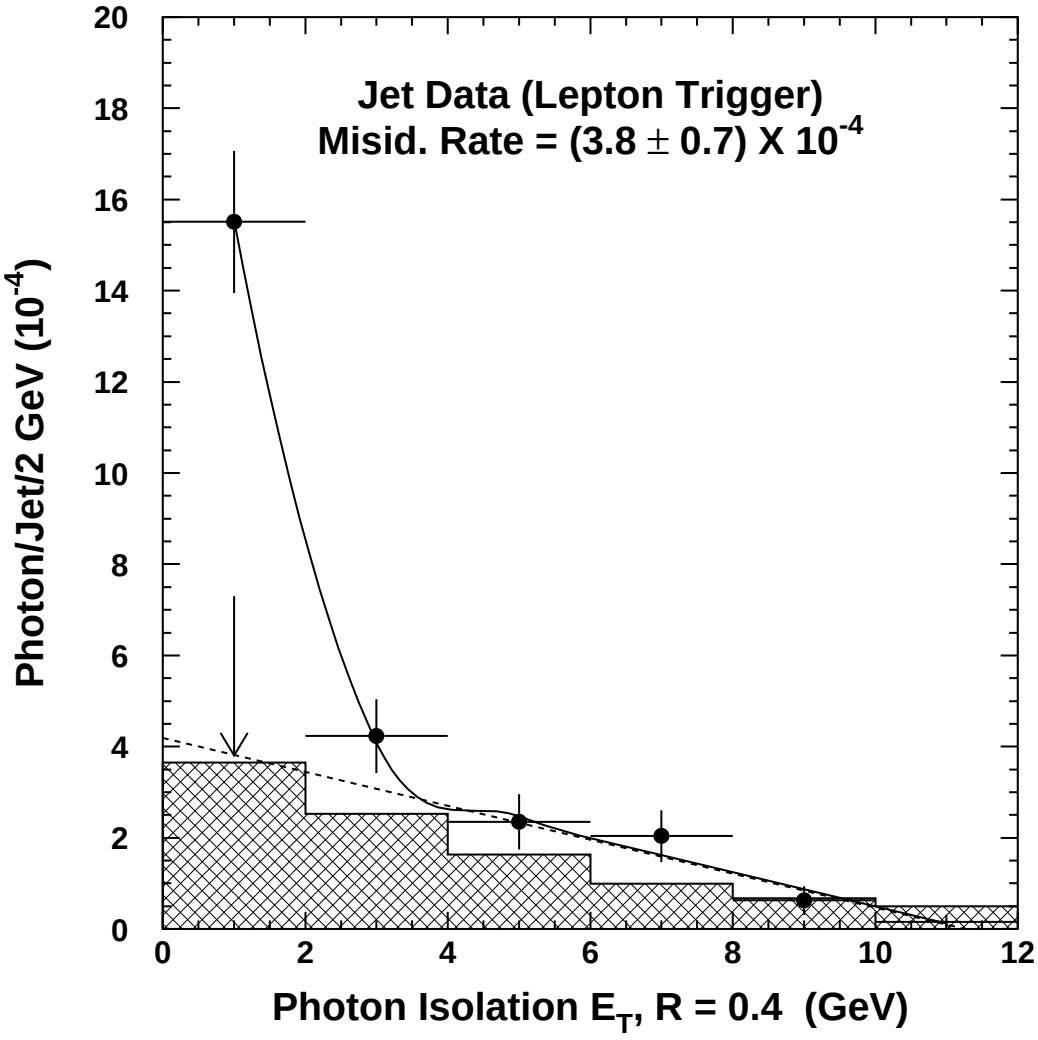

Figure 4.4: The number of photon candidates per jet, as a function of E_{cone}^{Iso}, for CDF jet data obtained with a lepton trigger. Included are the results of CDF data (points), the fit of CDF data to Equation 4.7 (solid line), the linear portion of the same fit (dotted line), and an estimate of this distribution from a simulation of W plus jet events performed by PYTHIA.

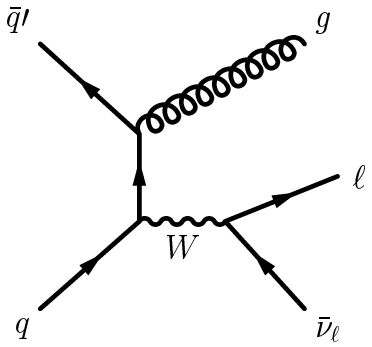

a) $q\bar{q}' \to Wg$

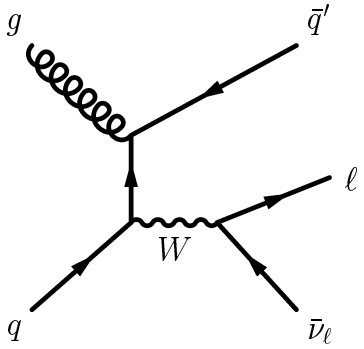

b) $qg \to W\bar{q}'$

Figure 4.5: The leading-order Feynman diagrams for W-jet production.

ton events and muon-triggered photon events separately. The separate jet misidentification rates obtained from these distributions, also shown in Table 4.7, are statistically consistent with each other.

Additional evidence for the linear behavior of $dN/d\mathrm{E}_{\mathrm{cone}}^{\mathrm{Iso}}$ in misidentified jets is obtained from a sample of lepton-triggered events enriched with π^0's. Lepton candidates in these lepton-triggered π^0 events are selected with the same trigger requirements as the lepton-triggered photon events described above. Lepton-triggered π^0 events are required to have exactly one loose lepton candidate as above, and are required to have exactly one π^0 candidate which satisfies requirements similar to photon candidates in Table 3.1, with the following differences: the isolation requirements are not applied, as done for the lepton-triggered photon sample; the requirements for additional CES energy clusters are not applied; and the χ^2_{Avg} is required to be *greater* than 20. The lepton-triggered π^0 sample consists of 38 electron-π^0 and 11 muon-π^0 events.

The distribution $dN/d\mathrm{E}_{\mathrm{cone}}^{\mathrm{Iso}}$ for lepton-triggered π^0 events is shown in Figure 4.7. The distribution (solid points) is consistent with that of a linearly decreasing tail. Also shown in Figure 4.7 is an estimate of $dN/d\mathrm{E}_{\mathrm{cone}}^{\mathrm{Iso}}$ obtained from a simulation of W-jet production (cross-hatched histogram) as described above, except with the lepton-triggered π^0 selection applied. As with lepton-triggered photons, the simulated results for $dN/d\mathrm{E}_{\mathrm{cone}}^{\mathrm{Iso}}$ exhibit a shape consistent with a linear functional form, as well as a magnitude consistent with the observed π^0 rate.

Table 4.8 shows the mean number of photon-lepton events expected to originate from misidentified jets, for the various subsets of photon-lepton events to be analyzed. The uncertainties in these estimates are dominated by the uncertainty in P_γ^{jet}, which in turn is limited in precision by the number of exclusive photon-lepton events. The

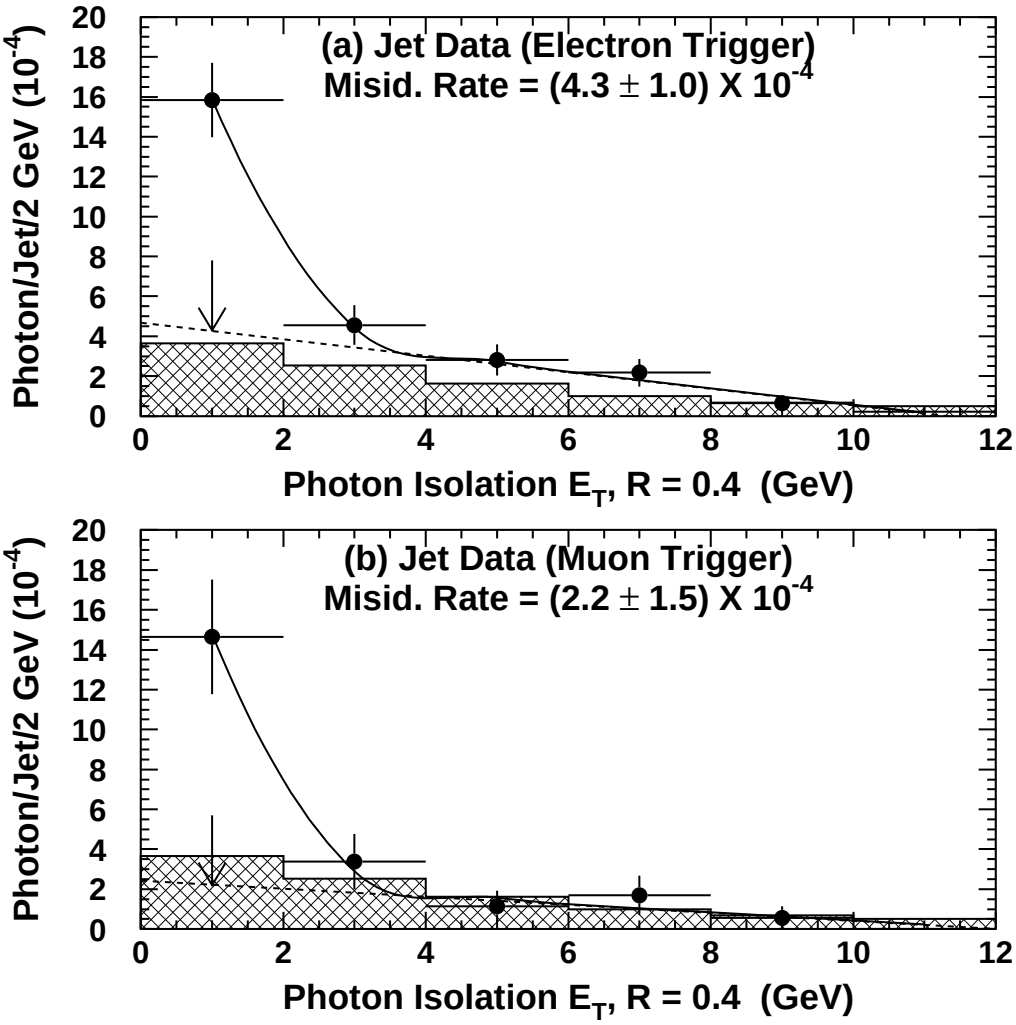

Figure 4.6: The number of photon candidates per jet, as a function of E_{cone}^{Iso}, for CDF jet data obtained with (a) an electron trigger or (b) a muon trigger. Included are the results of CDF data (points), the fit of CDF data to Equation 4.7 (solid line), the linear portion of the same fit (dotted line), and an estimate of this distribution from a simulation of W plus jet events performed by PYTHIA.

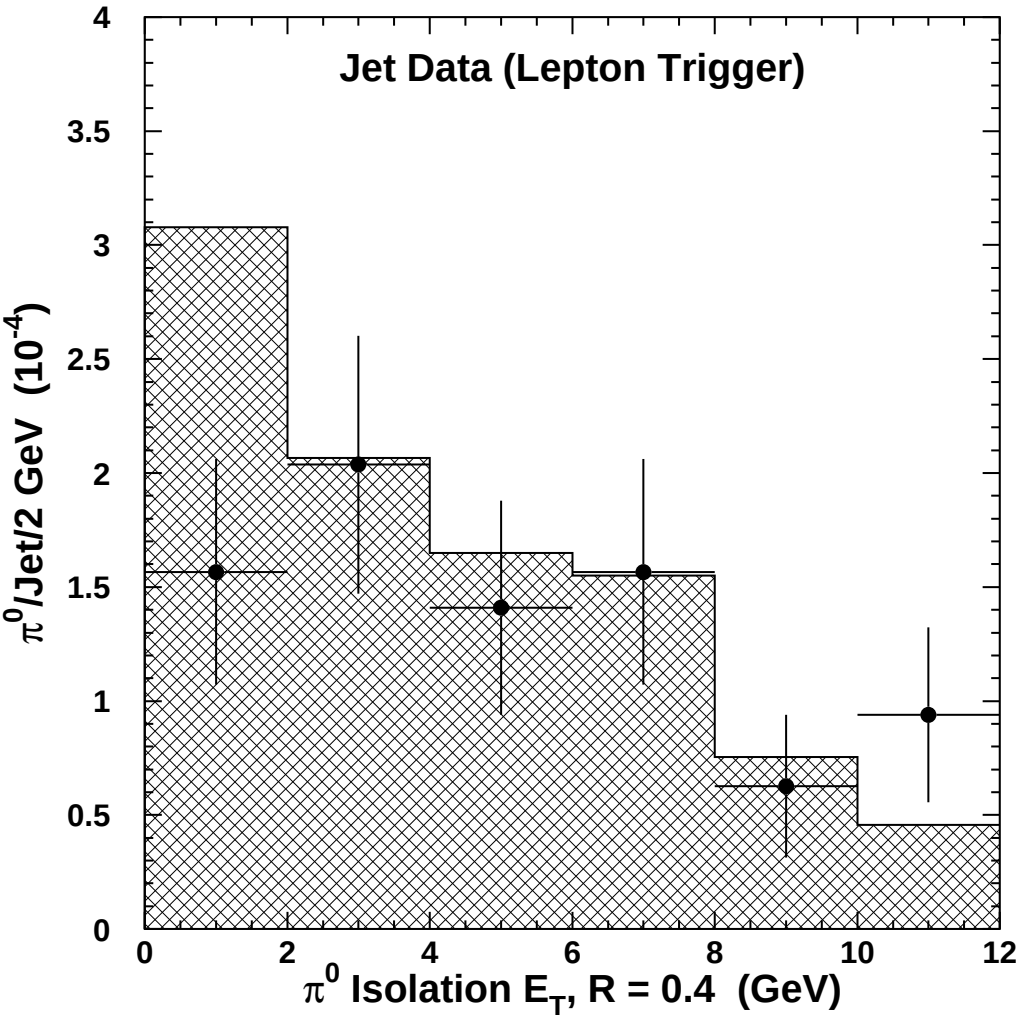

Figure 4.7: The number of π^0 candidates per jet, as a function of $\mathrm{E}_{\mathrm{cone}}^{\mathrm{Iso}}$, for CDF jet data obtained with a lepton trigger. Included are the results of CDF data (points), the fit of CDF data to Equation 4.7 (solid line), the linear portion of the same fit (dotted line), and an estimate of this distribution from a simulation of W plus jet events performed by PYTHIA.

	N_{raw}	$N_{\ell jet}$	$N_{\ell\gamma}$
Two-Body Events			
$e\gamma$	4530	4909	1.9 ± 0.3
$\mu\gamma$	1983	3844	1.5 ± 0.3
Multi-Body Events			
$e\gamma X$	4235	4565	1.7 ± 0.3
$\mu\gamma X$	2024	3855	1.5 ± 0.3
$e\gamma \not\!\!E_{\rm T}$	2584	2798	1.1 ± 0.2
$\mu\gamma \not\!\!E_{\rm T}$	1369	2633	1.0 ± 0.2
$ee\gamma$	479	496	0.19 ± 0.03
$\mu\mu\gamma$	226	346	0.13 ± 0.02
$e\mu\gamma$	16	19	—
$e\gamma\gamma$	3	3	—
$\mu\gamma\gamma$	3	4	—

Table 4.8: The contributions $N_{\ell\gamma}$ to the various categories of photon-lepton candidates from jets misidentified as photons, using the measured jet misidentification rate $3.8 \pm 0.7 \times 10^{-4}$. Included are the raw number N_{raw} of jets in inclusive lepton data and the effective number of jets $N_{\ell jet}$ which potentially contribute to each category.

total number of two-body and multi-body events expected is 1-2 events per category per lepton species, with roughly equal contributions in photon-electron and photon-muon events. The number of multi-lepton events arising from misidentified jets is an order of magnitude smaller. The number of $e\mu\gamma$, $e\gamma\gamma$, and $\mu\gamma\gamma$ events arising from misidentified jets is negligible, due to the small number of jets in $e\mu$, $e\gamma$, and $\mu\gamma$ events, respectively.

4.3 Electrons Misidentified as Photons

The dominant source of fake background for photon-electron events is $Z^0 \to e^+e^-$ production, wherein one of the electrons undergoes hard photon bremsstrahlung in the detector material, or the CTC fails to detect one of the electron tracks, and that electron subsequently passes all of the photon cuts. There are approximately 1000

central electron pairs in the CDF data, so a photon fake rate as low as 1% will give rise to 20 photon-electron background events, which would be unacceptably high for finding sources of new physics comparable to $W/Z^0 + \gamma$ production (see Tables 4.3–4.6). It is therefore necessary to either obtain independently the photon fake rate to sufficient accuracy that a background subtraction can be performed, or to assume that those photon-electron events in the CDF data which are sufficiently similar in their kinematics to Z^0 production are not a significant source of new physics, and that such events may be used to estimate the photon-electron background rate elsewhere. The latter method is employed in what follows.

A control sample of Z^0-like events is selected from the 49 two-body photon-electron candidates by requiring that the invariant mass of the photon-electron pair, $M_{e\gamma}$, be within 5 GeV of the Z^0 mass (91 GeV). There are 17 such events in the CDF data, and their characteristics are shown in Figure 4.8. In order to check the assumption that these are predominantly $Z^0 \to e^+e^-$ events, a sample of $Z^0 \to e^+e^-$ events is selected from the inclusive electron sample which have exactly two electrons passing the electron criteria in Table 3.3, and which have the same kinematic requirements as the photon-electron control sample. There are 1235 such events, and their distributions, normalized to the photon-electron control sample, are also shown in Figure 4.8. It is observed that the shapes of the distributions of the two samples are statistically consistent with each other.

Some of the photon-electron events in the control sample will arise from real photons from $W/Z^0 + \gamma$ production, or from photons misidentified as jets. In order to avoid double-counting these as a source of background, the diboson Monte Carlo calculations described in Chapter 4.1 and the jet misidentification calculations described in Chapter 4.2 are used to estimate the number of photon-electron events

passing the control sample cuts, and this is subtracted from the total number of control sample events to give a corrected rate for electron-fake-photon production. Out of 17 events, 1.24 ± 0.13 events (1.01 ± 0.12 from diboson events, 0.23 ± 0.04 from misidentified jets) on average are expected to have real photons, which are subtracted to give 15.8 ± 4.3 electron-fake-photon events in the control sample.

The number of electron-fake-photon control sample events, $N_{e\gamma}^{ctrl}$, divided by the number of electron-electron events with the same kinematics, N_{ee}^{ctrl}, gives the electron-fake-photon rate per central electron pair. This can then be applied to any particular subset of central electron pairs to give the electron-fake-photon rate for the corresponding photon-electron subset. For multi-body photon-lepton events, a sample of dielectron events is selected from events satisfying the same trigger criteria as that of the photon-electron candidates described in Chapter 3.3. From these triggers a sample of multi-body dielectron events is selected which has exactly two electrons passing the electron criteria in Table 3.3, and which has the same angular separation requirements ($\Delta\varphi_{ee} < 150°$) as the multi-body photon-lepton sample. There are 132 such events. The estimated number of electron-fake-photon events in multi-body photon-electron events is therefore

$$\begin{aligned} N_{e\gamma}^{mult} &= [(15.8 \pm 4.3)/1235] \times 132 \\ &= 1.7 \pm 0.5 \text{ events.} \end{aligned} \tag{4.8}$$

Similar calculations are made for the other photon-lepton samples analyzed, and the results are summarized in Table 4.9. The number of multi-photon and multi-lepton events is negligible, due to the low number of $ee\gamma$ and eee events in the CDF data.

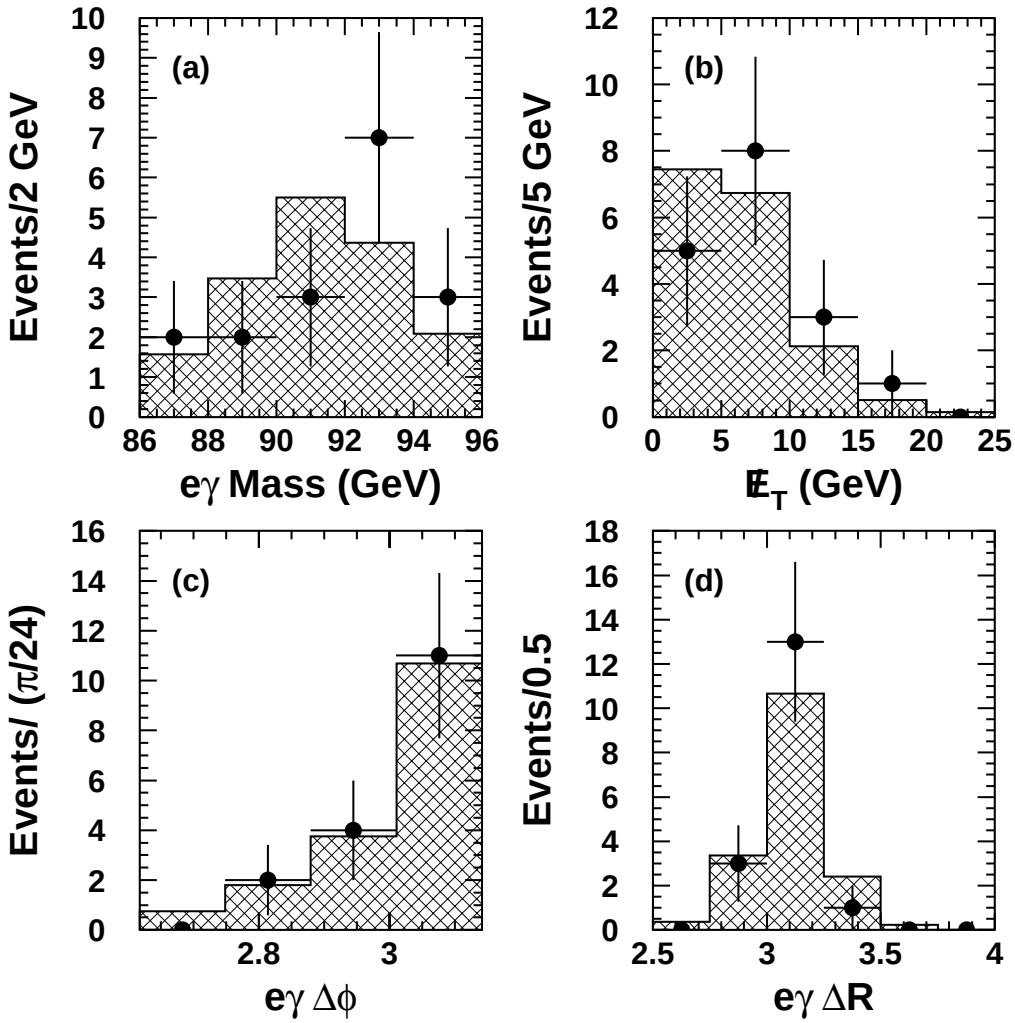

Figure 4.8: The distributions for (a) $M_{e\gamma}$, (b) $\not\!\!E_{\rm T}$, (c) $\Delta\varphi_{e\gamma}$, and (d) $\Delta R_{e\gamma}$ in Z^0-like events. The points are the Z^0-like photon-electron sample; the shaded histogram is electron-electron events from CDF data with the same kinematic cuts, normalized to the control sample.

	N_{ee}	$N_{e\gamma}$
Two-Body $e\gamma X$	321	4.10 ± 1.14
Multi-Body $e\gamma X$	132	1.68 ± 0.49
Multi-Body $e\gamma \not\!\!E_{\rm T}$	8	0.10 ± 0.04

Table 4.9: The expected mean number of photon-electron candidates $N_{e\gamma}$ from Z^0 electrons misidentified as photons, for the various categories analyzed. Included is the number of dielectron events N_{ee} which potentially contribute to each category.

4.4 Light Hadrons Misidentified as Muons

A hadron jet can contain charged hadrons, which may occasionally penetrate the calorimetry and be detected by the muon chambers, ("hadron punchthrough"), or which may decay to a muon before reaching the calorimetry ("hadron decay-in-flight"). If one of these hadrons constitutes a sufficiently large fraction of the jet momentum, then the hadron jet can be misidentified by the CDF detector as a single prompt muon. Such a jet produced in association with a photon candidate contributes to the detected photon-muon candidates. The contribution of photon plus misidentified jet events is determined by analyzing a sample of isolated, high-momentum tracks in CDF photon data, determining the probability of each track being misidentified as a muon, and computing the total contribution by summing this probability over all tracks in the sample.

Starting with the inclusive photon events described in Chapter 3.1, a photon-track sample is selected which satisfies the following criteria: one or more photon candidates satisfying the criteria in Table 3.1; and one or more CTC tracks which extrapolate to the CMU, CMP, or CMX detectors, with $p_T > 25$ GeV/c. The selected CTC tracks must also satisfy the same track requirements as those of muon tracks, as described in Chapter 3.2: a minimum of six layers of CTC wire measurements, at least three of which must be axial wire measurements and at least 2 of which must

be stereo wire measurements; an impact parameter $d_0 < 0.3$ cm; the distance in z of the CTC track to the primary event vertex $|\Delta z_{event}| < 5$ cm; and, as an isolation requirement, the sum of the momenta of other CTC tracks incident upon a cone of $R = 0.4$ around the candidate track direction must be less than 10% of the $\mathrm{p_T}$ of the candidate track. The photon-track sample consists of 394 events containing 398 track candidates.

Because the photon trigger requirements of the photon-track sample are less efficient than the trigger requirements of the photon-muon sample, the effective number of tracks which potentially contribute to the photon-muon candidates must be augmented by a ratio of the efficiencies of the different trigger paths, for each track in each event of the sample. The efficiency ratio $R_{\gamma t}$ varies with photon $\mathrm{E_T}$ and the muon stub type μ_i that the track t would produce in the event of hadron punchthrough or decay-in-flight:

$$R_{\gamma t} = \frac{\epsilon_{\mu_i} + (1 - \epsilon_{\mu_i}) \times \epsilon_\gamma(\mathrm{E_T})}{\epsilon_\gamma(\mathrm{E_T})}, \tag{4.9}$$

where ϵ_{μ_i} is the trigger efficiency for muons of stub type i, and $\epsilon_\gamma(\mathrm{E_T})$ is the trigger efficiency of photon candidates as a function of photon $\mathrm{E_T}$.

The fraction of track candidates which give rise to hadron punchthrough is computed from the number of hadronic interaction lengths traversed through the calorimeter to a muon chamber, for high-momentum pions and kaons. The thickness of the CDF calorimeter, typically 5 absorption lengths for pions (4.4 for kaons), corresponds to a hadron rejection factor of about 150 (80) for the CMU and CMX. The CMP is additionally shielded from hadrons by 60 cm of steel, which effectively absorbs all incident hadrons; the contribution of hadron punchthrough to CMP or CMUP muon candidates is henceforth assumed to be negligible. For each track in the

Stub Type	Two-Body $\mu\gamma X$	Multi-Body $\mu\gamma X$	Multi-Body $\mu\gamma \not{E}_{\rm T}$
CMUP	—	—	—
CMNP	0.37	0.12	0.07
CMX	0.15	0.08	0.03
CMP	—	—	—
CMU	0.90	0.25	0.09
Total	1.42 ± 0.74	0.45 ± 0.25	0.18 ± 0.11

Table 4.10: The contribution to the photon-muon candidates of punchthrough hadrons misidentified as muons, indexed by muon stub type, for various categories analyzed.

photon-track sample, the probability of the track becoming hadron punchthrough, $P^t_{PT\mu}$, is given by

$$\begin{aligned} P^t_{PT\mu} &= F_\pi \times \exp\left(-\lambda_\pi(E^t)/\sin\theta_t\right) \\ &\quad + F_K \times \exp\left(-\lambda_K(E^t)/\sin\theta_t\right), \end{aligned} \tag{4.10}$$

where F_π and F_K are the relative $\pi : K$ fractions; and $\lambda_\pi(E^t)$ and $\lambda_K(E^t)$ are the calorimeter thicknesses in units of the interaction lengths for the corresponding particle type, as a function of the total energy E^t of the track t and the sign of its charge. The interaction length for kaons is longer than that of pions, so $P_{PT\mu}$ is a maximum for $F_K = 1.0$ and a minimum for $F_K = 0.0$. For the central value estimate, an experimentally measured value $F_K = 0.33$ is used [26], with upper and lower systematic bounds defined by $F_K = 1.0$ and $F_K = 0.0$. This systematic uncertainty is the dominant uncertainty for the hadron punchthrough estimates.

For any particular subset of the photon-track sample, the total contribution to the corresponding photon-muon sample is the sum over all candidate tracks of the hadron punchthrough probabilities, weighted by the appropriate trigger efficiency

ratio for each track:

$$N_{PT\mu} = \sum_t R_{\gamma t} \times P^t_{PT\mu}. \tag{4.11}$$

For example, in the case of multi-body $\mu\gamma$ events, a subset of the punchthrough candidates is selected for which the track extrapolates to the CMU or CMX detectors, and $\Delta\varphi$ between the photon and the track is less than 150°. There are 89 such tracks, corresponding to a background of $0.45^{+0.25}_{-0.13}$ events from hadron punchthrough in the inclusive multi-body $\mu\gamma$ sample. Of these 89 tracks, 32 belong to events with $\not\!\!E_{\rm T} > 25$ GeV, corresponding to $0.18^{+0.11}_{-0.06}$ punchthrough events in the multi-body $\mu\gamma\not\!\!E_{\rm T}$ sample. The results indexed by muon stub type are shown in Table 4.10.

Each of the photon-track events described above is also a potential contribution to photon-muon events in the form of hadron decay-in-flight; hadrons which decay to muons prior to interacting with the central calorimeters will satisfy the requirements of prompt muons. The inner radius of the central calorimeters is 1.73 m, and the radius corresponding to one hadronic interaction length is approximately 2 m; hadrons decaying prior to a radius of 2 m are therefore likely to be misidentified as muons.

For each track in the photon-track sample, the hadron decay-in-flight probability $P^t_{DIF\mu}$ is given by

$$\begin{aligned} P^t_{DIF\mu} = {} & F_\pi \times {\rm B}R(\pi^\pm \to \mu\nu) \\ & \times(1 - \exp\left(-(2.0/c\tau_\pi)(m_\pi/c{\rm p_T})\right)) \\ & + F_K \times {\rm B}R(K^\pm \to \mu\nu) \\ & \times(1 - \exp\left(-(2.0/c\tau_K)(m_K/c{\rm p_T})\right)), \end{aligned} \tag{4.12}$$

where p_T is the transverse momentum of the track t, in GeV/c; F_π is the fraction of tracks which are pions, BR($\pi^\pm \to \mu\nu$) is the branching ratio of pions to muons (~ 1.0), $c\tau_\pi$ is the pion proper decay length in meters (7.8 m), and m_π is the pion mass (0.140 GeV); F_K is the fraction of tracks which are kaons, BR($K^\pm \to \mu\nu$) is the branching ratio of kaons to muons (0.635), $c\tau_K$ is the kaon proper decay length in meters (3.7 m), and m_K is the kaon mass (0.494 GeV). For tracks with transverse momentum of 25 GeV/c, the decay-in-flight probability is 0.67% for kaons and 0.14% for pions.

For any particular subset of the photon-track sample, the contribution to the corresponding photon-muon candidates of decay-in-flight hadrons is the sum over all tracks of the decay-in-flight probabilities, augmented by the trigger efficiency ratio:

$$N_{DIF\mu} = \sum_t R_{\gamma t} \times P^t_{DIF\mu} \tag{4.13}$$

Due to the shorter kaon lifetime, the upper and lower bounds are again determined by the results assuming kaon fractions of 1.0 and 0.0, respectively, with the central value determined by $F_K = 0.33$. The results indexed by muon stub type are shown in Table 4.11. The contributions relative to those sources of photon-muon events considered previously are small.

4.5 Heavy-Flavored Hadron Decay to Leptons

A hadron consisting of one or more quarks with heavy flavor (charm or bottom) has a much shorter lifetime than those hadrons considered in Section 4.4; at the Tevatron, heavy-flavored hadrons typically travel a few millimeters before decaying and do not produce a measurable track in the CTC. Consequently, the decay in

Stub Type	Two-Body $\mu\gamma X$	Multi-Body $\mu\gamma X$	Multi-Body $\mu\gamma \not\!\!E_{\rm T}$
CMUP	0.35	0.10	0.03
CMNP	0.15	0.04	0.02
CMX	0.21	0.11	0.03
CMP	0.08	0.04	0.01
CMU	—	—	—
Total	0.80 ± 0.89	0.28 ± 0.31	0.10 ± 0.11

Table 4.11: The contribution to the photon-muon candidates of decay-in-flight hadrons misidentified as muons, indexed by muon stub type, for the various categories analyzed.

flight of heavy-flavored hadrons to leptons is not accounted for in the estimates of Section 4.4, which infer the number of decay-in-flight hadrons from CTC tracks. The contribution to photon-lepton candidates that arises from heavy-flavored hadrons produced in association with a prompt photon is instead accounted for through Monte Carlo event generation and detector simulation, as in Section 4.1.

Figure 4.9 shows the leading-order Feynman diagram for a heavy-flavored quark produced in association with a prompt photon. The leading-order matrix element for this process is calculated with the PYTHIA [18] event generator program, using the leading-order proton structure function CTEQ5L [19]. PYTHIA also generates, fragments, and hadronizes the partons produced in a simulated interaction. The QQ program, based on measurements of the CLEO experiment [27], is used to compute the decays of heavy-flavored hadrons. Previous measurements of photon-heavy-flavor events at the Tevatron [28] indicate agreement of CDF data with next-to-leading order QCD predictions. In order to obtain agreement of the leading order simulation with next-to-leading order cross section predictions, a next-to-leading order K-factor is applied to the leading order cross section computed by PYTHIA. In the previous measurements this K-factor was found to be $K_{NLO} = 1.9 \pm 0.2$. Using this K-factor

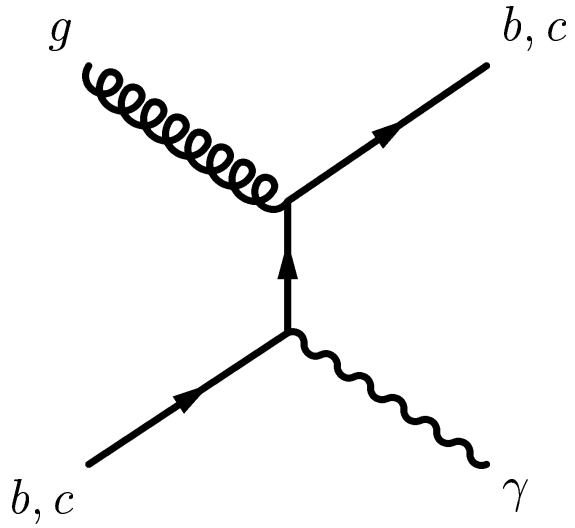

Figure 4.9: The leading-order Feynman diagram for $\gamma + b, c$ production.

and the leading-order cross section computed by PYTHIA ($\sigma_{LO} = 7$ nb), the mean contribution to photon-lepton candidates in CDF data for this process is given by Equation 4.2 in Section 4.1.

Table 4.12 shows, for the various signal regions of this analysis, the number of simulated events which are photon-lepton candidates, N_{MC}, out of 117 million events (equivalent to 8.4 fb^{-1}) generated; and the mean contribution expected in 86.34 pb^{-1} of CDF data, $N_{\ell\gamma}$. The contributions expected are small compared to those discussed in Sections 4.1–4.4. All simulated candidates are found to be two-body photon-lepton events, as would be expected for a process with a two-body final state. Contributions to multi-body photon-lepton events are bounded from above by 0.01 at the 68% confidence level, and are henceforth assumed to be negligible.

	N_{MC} (8.4 fb^{-1})	$N_{\ell\gamma}$
Two-Body Events		
$e\gamma$	10	0.07 ± 0.02
$\mu\gamma$	3	0.03 ± 0.01
Multi-Body Events		
$e\gamma X$	0	< 0.01
$\mu\gamma X$	0	< 0.01
$e\gamma \not{E}_{\rm T}$	0	< 0.01
$\mu\gamma \not{E}_{\rm T}$	0	< 0.01

Table 4.12: The contribution to photon-lepton candidates, $N_{\ell\gamma}$, of heavy-flavored hadrons decaying to leptons, for the various categories analyzed. Included is the number of candidate events N_{MC} produced by the simulation for each category.

CHAPTER 5

ANALYSIS OF PHOTON-LEPTON CANDIDATES

The objectives of this analysis are the comparison of the total observed event rates, in the various photon-lepton samples described in Chapter 3.5, with the total rates predicted by the standard model, and a similar comparison of the distributions of kinematic properties in those samples. For each photon-lepton sample, the total mean rate predicted by the standard model, μ_{SM}, is the sum of each of the sources discussed in Chapter 4. The uncertainty in the total mean rate is the standard deviation of a large ensemble of calculations of the total predicted rate, where each of the quantities used to compute photon-lepton event sources (simulation systematics, integrated luminosity, photon and lepton misidentification rates, etc.) is allowed to fluctuate with a Gaussian distribution about its mean value. This ensemble of calculations accounts for correlated uncertainties between the various contributing sources, such as the uncertainty in the integrated luminosity used to normalize the various simulated event rates.

Also of interest, for the small samples dealt with here, is the probability that the total mean rate μ_{SM} predicted by the standard model would vary as a Poisson statistic up to or above (down to or below) any excess (deficit) level observed in CDF data, N_0. This "one-sided fluctuation probability", denoted by $P(N \geq N_0|\mu_{SM})$ for an observation of an excess over the predicted mean and $P(N \leq N_0|\mu_{SM})$ for observation of a deficit under the predicted mean, is again computed from a large ensemble of calculations of the total predicted rate. Each of the quantities used to compute photon-lepton sources is allowed to fluctuate with a Gaussian distribution

about its mean value, and the resulting mean is used to generate a Poisson distributed outcome N. The one-sided fluctuation probability is the fraction of outcomes in the ensemble which equal or exceed (equal or fall short of) the observed excess (deficit) in CDF data. Perfect agreement between the standard model and CDF data will yield a one-sided fluctuation probability of $\sim 50\%$, in some cases exceeding 50% due to the asymmetry about the mean of a Poisson distribution.

The total standard model predictions for the distributions of kinematic properties are the sums of the distributions of the corresponding properties of each of the sources discussed in Chapter 4. For the contribution from jets misidentified as photons, the appropriately weighted distributions of jet properties in lepton-jet events are used in the predicted distributions of photon properties. Similarly, for the contribution from electrons misidentified as photons the distributions of electron properties in electron-electron events are used to predict distributions of photon properties, and for the contribution from hadrons misidentified as muons the distributions of track properties in photon-track events are used to predict distributions of muon properties. The kinematic properties of the individual photon-lepton candidate events are tabulated in Appendix C.

5.1 Two-Body and Inclusive Multi-Body Photon-Lepton Events

The predicted and observed total rates for two-body photon-lepton events are compared in Table 5.1. The mean predicted contributions from each of the sources discussed in Chapter 4 are also listed. Half of the total predicted rate originates from $Z^0\gamma$ production where one of the charged leptons has evaded identification; the other half originates from roughly equal contributions of $W\gamma$ production, misiden-

Process	$e\gamma$	$\mu\gamma$	$\ell\gamma$
W+γ	1.17 ± 0.15	1.52 ± 0.21	2.69 ± 0.32
Z+γ	5.40 ± 0.57	7.06 ± 0.82	12.46 ± 1.21
ℓ+jet, jet $\rightarrow \gamma$	1.87 ± 0.34	1.46 ± 0.27	3.33 ± 0.72
$Z \rightarrow ee, e \rightarrow \gamma$	4.10 ± 1.14	-	4.10 ± 1.14
Hadron+γ	-	1.42 ± 0.74	1.42 ± 0.74
π/K Decay+γ	-	0.80 ± 0.89	0.80 ± 0.89
b/c Decay+γ	0.07 ± 0.02	0.03 ± 0.01	0.10 ± 0.03
Mean Rate μ_{SM}	12.61 ± 1.37	12.29 ± 1.78	24.90 ± 2.43
CDF Data N_0	20	13	33
$P(N \geq N_0 \mid \mu_{SM})$	0.043	0.46	0.093

Table 5.1: The mean rate μ_{SM} predicted by the standard model for two-body photon-lepton events, the number N_0 observed in CDF data, and the one-sided fluctuation probability $P(N \geq N_0 \mid \mu_{SM})$. There exist correlated uncertainties between the different photon-lepton sources.

tified jets, misidentified electrons, and misidentified charged hadrons. The total observed photon-electron rate is somewhat higher than the predicted rate, with an upward fluctuation probability of 4.3%; the observed photon-muon rate is in excellent agreement with the predicted rate, however, so that the upward fluctuation probability of the total two-body photon-lepton rate increases to 9.3%. The probability that the 33 total observed events would exhibit an asymmetry between electrons and muons of (20-13)/33 = 21% or greater where none is expected, is 30%.

The predicted and observed distributions of the kinematic properties of two-body photon-lepton events are compared in Figures 5.1 and 5.3. Superimposed upon the distributions of the total standard model contribution are the distributions of that portion arising from standard model diboson production.

Figure 5.1 shows the distributions of photon E_T, lepton E_T, and $\not\!\!E_T$ for the events. Observed photon and lepton E_T exhibit the range of values expected from the standard model. The number of two-body photon-lepton events observed with

$\not\!\!E_T < 25$ GeV is in good agreement with the predicted rate. There are 5 events observed with $\not\!\!E_T > 25$ GeV, whereas 2.3 events are expected, a result which is potentially related to that observed in multi-body $\ell\gamma\not\!\!E_T$ events described below.

The distribution of the total E_T of all objects in the event, H_T, is also included in Figure 5.1. It is defined as the sum of the magnitudes of $\not\!\!E_T$ and the transverse energies of all electrons, muons, photons, and jets in the event:

$$H_T \equiv \not\!\!E_T + \sum_e E_T^e + \sum_\mu cp_T^\mu + \sum_\gamma E_T^\gamma + \sum_j E_{T\ cor}^j. \tag{5.1}$$

The jets included in this sum are required to have $E_{T\ raw}^j > 8$ GeV and $|\eta_j| < 2.4$, just as in Equation 3.4. Large H_T is correlated with the production of massive particles, virtual or real. The observed data exhibit the range of H_T values expected.

Process	$e\gamma$	$\mu\gamma$	$\ell\gamma$
W+γ	2.44 ± 0.32	2.53 ± 0.34	4.97 ± 0.59
Z+γ	5.01 ± 0.54	4.60 ± 0.54	9.61 ± 0.94
ℓ+jet, jet $\to \gamma$	1.73 ± 0.32	1.46 ± 0.27	3.19 ± 0.59
$Z \to ee, e \to \gamma$	1.68 ± 0.49	-	1.68 ± 0.49
Hadron+γ	-	0.45 ± 0.25	0.45 ± 0.25
π/K Decay+γ	-	0.28 ± 0.31	0.28 ± 0.31
b/c Decay+γ	< 0.01	< 0.01	< 0.01
Mean Rate μ_{SM}	10.87 ± 0.97	9.33 ± 1.00	20.19 ± 1.66
CDF Data N_0	11	16	27
$P(N \geq N_0 \mid \mu_{SM})$	0.52	0.037	0.10

Table 5.2: The mean rate μ_{SM} predicted by the standard model for inclusive multi-body photon-lepton events, the number N_0 observed in CDF data, and the one-sided fluctuation probability $P(N \geq N_0 \mid \mu_{SM})$. There exist correlated uncertainties between the different photon-lepton sources.

The predicted and observed total rates for inclusive multi-body photon-lepton events are compared in Table 5.2. The magnitude of the predicted rate is similar

to that of two-body photon-lepton events. About half of the total predicted rate originates from $Z^0\gamma$ production, a quarter from $W\gamma$ production, and the remaining quarter from particles misidentified as photons or leptons. In this sample the total observed photon-muon rate is higher than the predicted rate, with an upward fluctuation probability of 3.7%; all of the difference can be attributed to events with large $\not\!\!E_{\rm T}$, as discussed below. The observed photon-electron rate is in excellent agreement with the predicted rate, and the upward fluctuation probability of the total two-body photon-lepton rate increases to 10%.

The predicted and observed distributions of the kinematic properties of inclusive multi-body photon-lepton events are compared in Figures 5.2 and 5.3. The difference between the observed and predicted rate can be entirely attributed to events with $\not\!\!E_{\rm T} > 25$ GeV; the observed events with lower $\not\!\!E_{\rm T}$ agree with predictions. There is also a larger proportion of observed events than expected with smaller photon-lepton azimuthal separation, $\Delta\varphi_{\ell\gamma}$, for which the contributions from misidentified photons or leptons are largely absent. Included in the observed multi-body photon lepton events is the $ee\gamma\gamma\not\!\!E_{\rm T}$ event previously analyzed by CDF [2] (Run 68739/Event 257646 in Appendix C).

5.2 Multi-Body $\ell\gamma\not\!\!E_{\rm T}$ Events

The predicted and observed total rates for multi-body $\ell\gamma\not\!\!E_{\rm T}$ events are compared in Table 5.3. For photon-electron events, requiring $\not\!\!E_{\rm T} > 25$ GeV suppresses the contribution from $Z^0\gamma$ production and from electrons misidentified as photons, which have no intrinsic $\not\!\!E_{\rm T}$, while preserving the contribution from $W\gamma$ production. As a result, 57% of the predicted $e\gamma\not\!\!E_{\rm T}$ rate arises from $W\gamma$ production, 31% from jets misidentified as photons, only 3% from $Z^0\gamma$ production, and the remaining 9% from

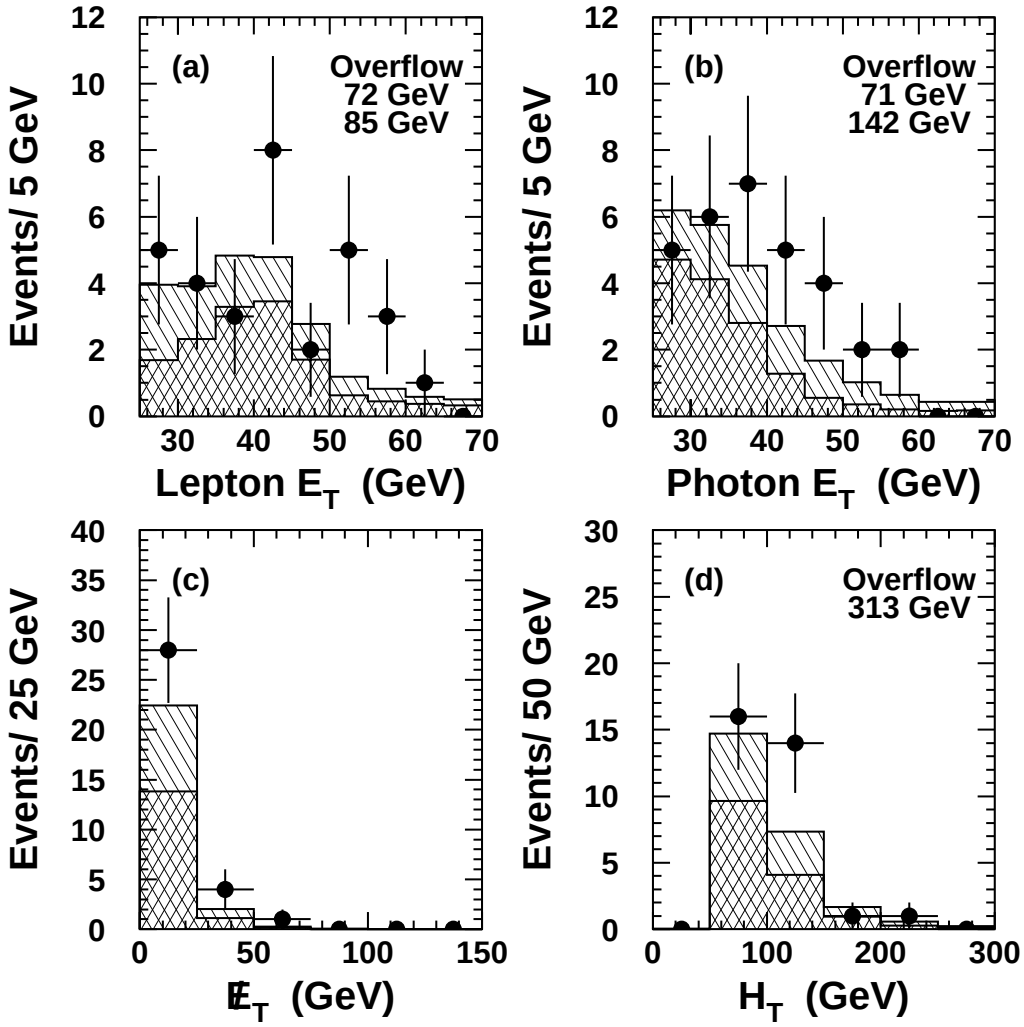

Figure 5.1: The distributions for (a) lepton E_T, (b) photon E_T, (c) $\not\!\!E_T$, and (d) H_T in two-body photon-lepton events. The points are CDF data, the hatched histogram is the total predicted mean background, and the cross-hatched histogram is the predicted mean diboson background.

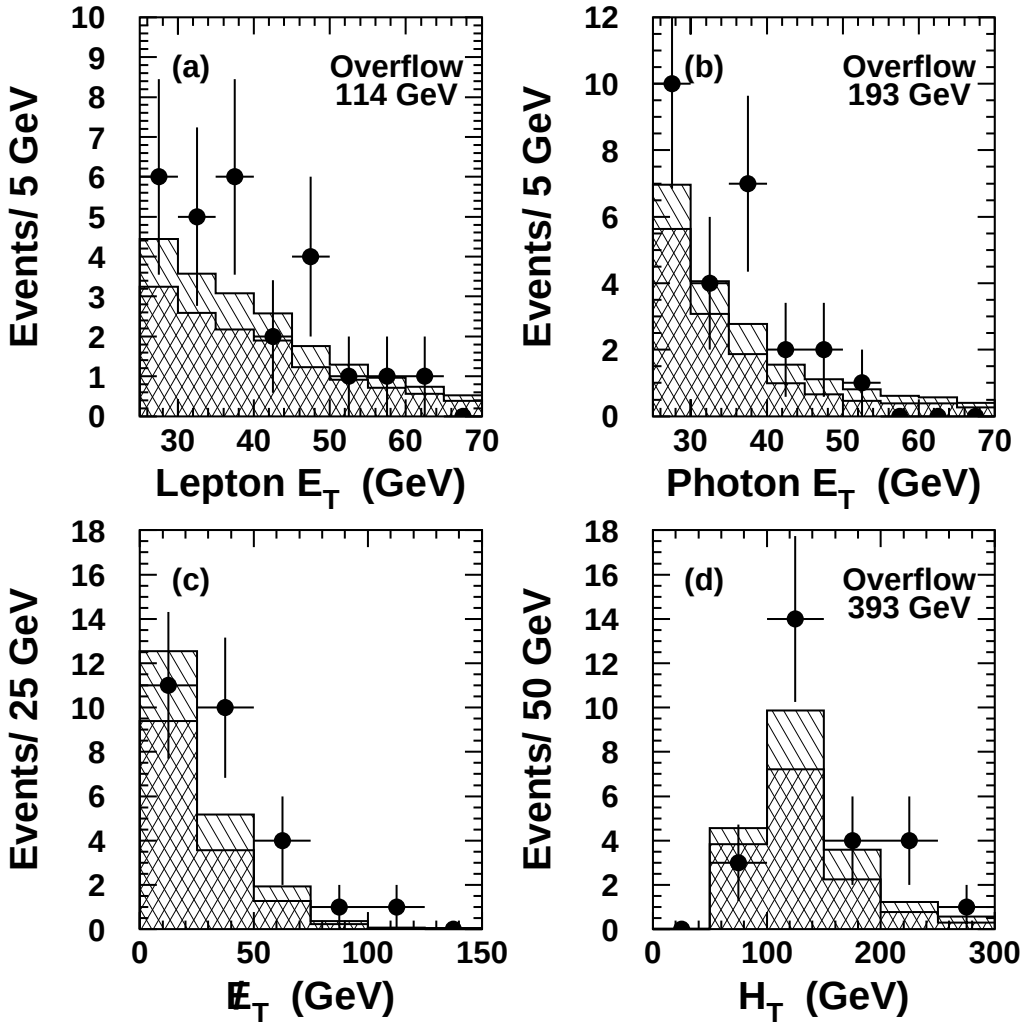

Figure 5.2: The distributions for (a) lepton E_T, (b) photon E_T, (c) $\not\!\!E_T$, and (d) H_T in inclusive multi-body photon-lepton events. The points are CDF data, the hatched histogram is the total predicted mean background, and the cross-hatched histogram is the predicted mean diboson background.

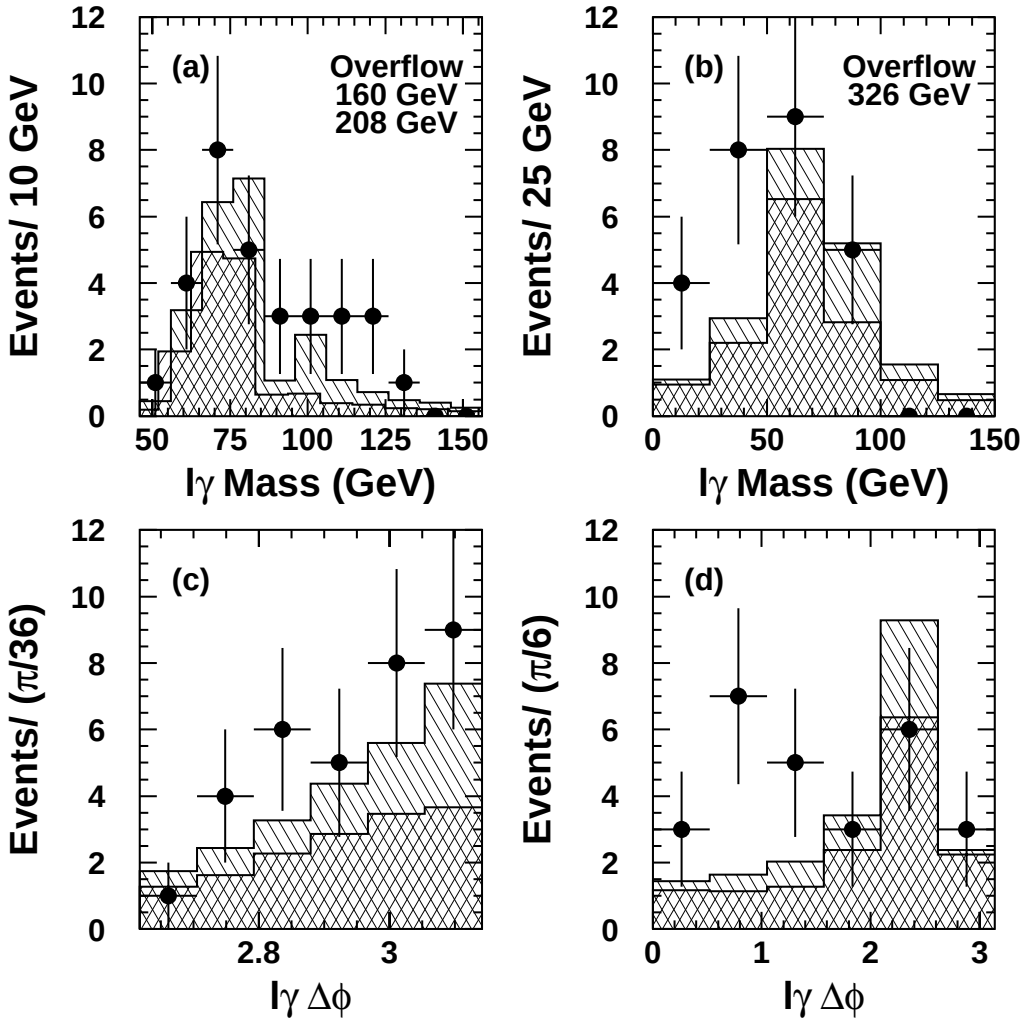

Figure 5.3: The distributions for (a) $M_{\ell\gamma}$ in two-body photon-lepton events, (b) $M_{\ell\gamma}$ in inclusive multi-body photon-lepton events, (c) $\Delta\varphi_{\ell\gamma}$ in two-body photon-lepton events, and (d) $\Delta\varphi_{\ell\gamma}$ in inclusive multi-body photon-lepton events. The points are CDF data, the hatched histogram is the total predicted mean background, and the cross-hatched histogram is the predicted mean diboson background.

other particles misidentified as photons. The observed $e\gamma\not\!\!E_{\rm T}$ rate agrees with the predicted rate, with a 25% probability that the predicted mean rate of 3.4 events yields 5 observed events. Included in the 5 events observed is the $ee\gamma\gamma\not\!\!E_{\rm T}$ event.

For photon-muon events, requiring $\not\!\!E_{\rm T} > 25$ GeV does not completely eliminate the contribution from $Z^0\gamma$, for if the second muon has $|\eta| > 1.2$ and $\rm p_T > 25$ GeV/c it evades all forms of muon detection and induces the necessary amount of $\not\!\!E_{\rm T}$. The rate at which this occurs is estimated well by $Z^0\gamma$ event simulation, however, since it is solely a function of the CDF detector acceptance for such a second muon. Of the 4.6 multi-body photon-muon events predicted to originate from $Z^0\gamma$ production, 2.2 events are predicted to contain a second visible muon, 1.0 are predicted to induce more than 25 GeV of $\not\!\!E_{\rm T}$ as above, and 1.4 are predicted to induce less than 25 GeV of $\not\!\!E_{\rm T}$. As shown in Table 5.4, 1 event is observed with a second visible muon, in agreement with $Z^0\gamma$ predictions. The total predicted rate for multi-body $\mu\gamma\not\!\!E_{\rm T}$ events consists of 47% $W\gamma$ production, 24% events with jets misidentified as photons, 23% $Z^0\gamma$ production, and the remaining 7% from other particles misidentified as muons.

The total observed $\mu\gamma\not\!\!E_{\rm T}$ rate is much higher than the predicted rate (11 observed vs. 4 expected), with an upward fluctuation probability of only 0.54%; the upward fluctuation probability of the total $\ell\gamma\not\!\!E_{\rm T}$ rate is only slightly higher at 0.72%. The probability that the 16 total observed events would exhibit an asymmetry between muons and electrons of (11-5)/16 = 37.5% or greater where none is expected, is 7.7%, so it is reasonable to interpret the difference in expected and observed rates as arising from the total rate and not from the muon channel alone.

The predicted and observed distributions of the kinematic properties of multi-body $\ell\gamma\not\!\!E_{\rm T}$ events are compared in Figures 5.4–5.6. The photon $\rm E_T$, lepton $\rm E_T$,

Process	$e\gamma\not\!\!E_{\rm T}$	$\mu\gamma\not\!\!E_{\rm T}$	$\ell\gamma\not\!\!E_{\rm T}$
W+γ	1.93 ± 0.26	1.99 ± 0.27	3.92 ± 0.47
Z+γ	0.32 ± 0.05	0.96 ± 0.15	1.27 ± 0.17
ℓ+jet, jet $\rightarrow \gamma$	1.06 ± 0.20	1.00 ± 0.18	2.06 ± 0.38
$Z \rightarrow ee, e \rightarrow \gamma$	0.10 ± 0.04	-	0.10 ± 0.04
Hadron+γ	-	0.18 ± 0.11	0.18 ± 0.11
π/K Decay+γ	-	0.10 ± 0.11	0.10 ± 0.11
b/c Decay+γ	< 0.01	< 0.01	< 0.01
Mean Rate μ_{SM}	3.41 ± 0.34	4.23 ± 0.46	7.64 ± 0.71
CDF Data N_0	5	11	16
$P(N \geq N_0 \mid \mu_{SM})$	0.26	0.0054	0.0072

Table 5.3: The mean rate μ_{SM} predicted by the standard model for multi-body $\ell\gamma\not\!\!E_{\rm T}$ events, the number N_0 observed in CDF data, and the one-sided fluctuation probability $P(N \geq N_0 \mid \mu_{SM})$. There exist correlated uncertainties between the different photon-lepton sources.

$\not\!\!E_{\rm T}$, and $H_{\rm T}$ observed are within the range expected from the standard model. The observed photon $E_{\rm T}$ spectrum has more events near the 25 GeV threshold than expected. However, nearly all photon candidates are one standard deviation or more above threshold in terms of the 3% CEM energy resolution (see Appendix C). The masses of combinations of objects in observed $\ell\gamma\not\!\!E_{\rm T}$ events are characterized by photon-lepton mass less than 100 GeV, lepton-$\not\!\!E_{\rm T}$ transverse mass greater than 50 GeV, photon-$\not\!\!E_{\rm T}$ transverse mass between 80 and 100 GeV, and $\ell\gamma\not\!\!E_{\rm T}$ transverse mass between 90 and 120 GeV. The observed angular distributions favor smaller azimuthal photon-lepton separation and larger lepton-$\not\!\!E_{\rm T}$ and photon-$\not\!\!E_{\rm T}$ azimuthal separations than expected from the standard model. The difference in total rate is therefore difficult to attribute to misidentified photons or leptons, which as shown in Figure 5.6 tend to have the larger photon-lepton azimuthal separation that is characteristic of a two-body final state.

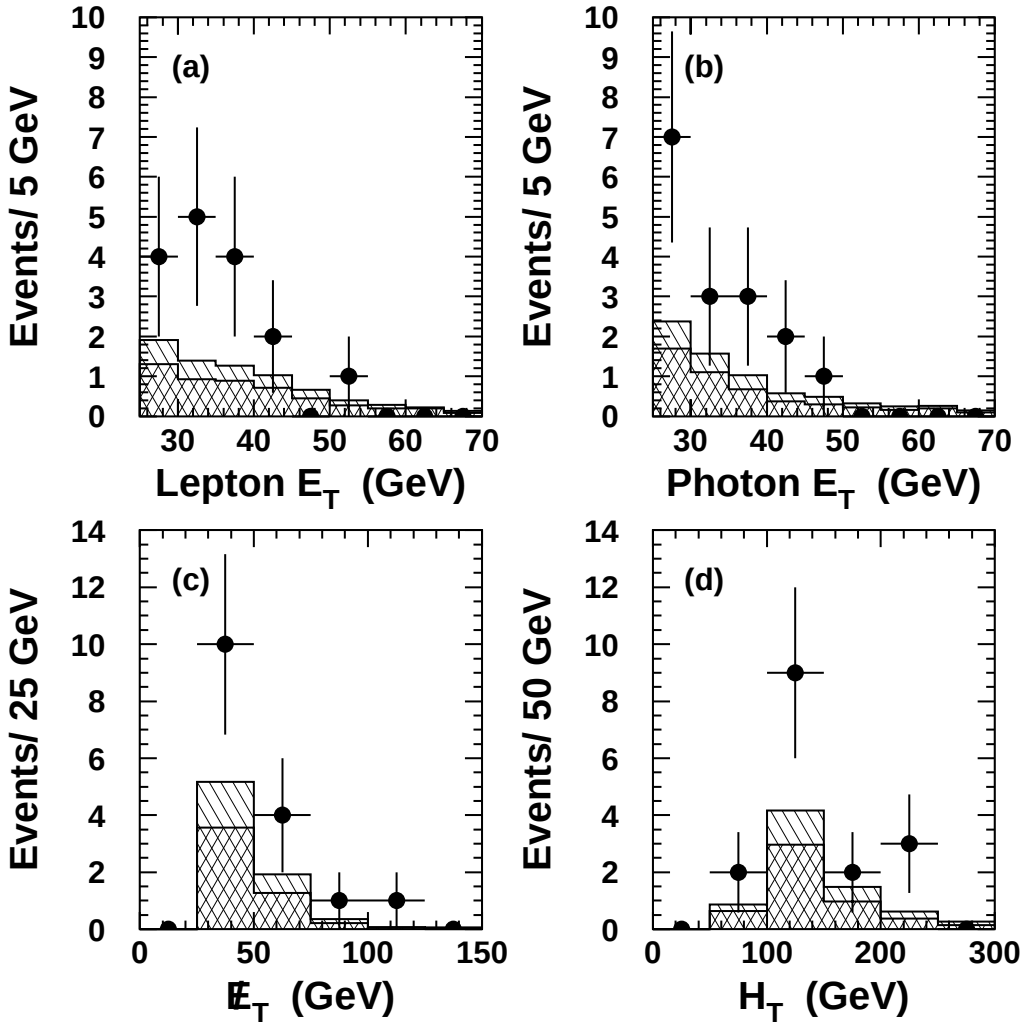

Figure 5.4: The distributions for (a) lepton E_T, (b) photon E_T, (c) $\not\!\!E_T$, and (d) H_T in multi-body $\ell\gamma\not\!\!E_T$ events. The points are CDF data, the hatched histogram is the total predicted mean background, and the cross-hatched histogram is the predicted mean diboson background.

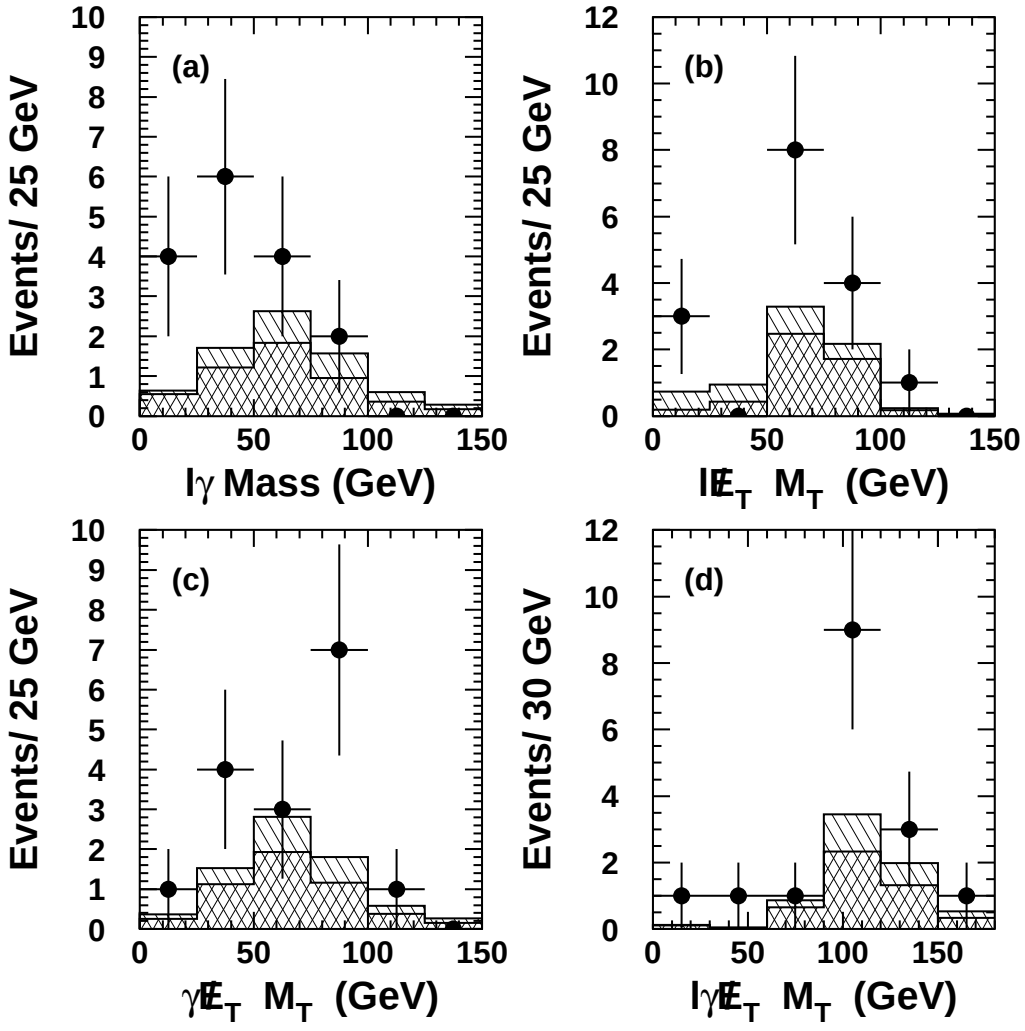

Figure 5.5: The distributions for (a) photon-lepton mass, (b) lepton-$\not\!\!E_{\rm T}$ transverse mass, (c) photon-$\not\!\!E_{\rm T}$ transverse mass, and (d) $\ell\gamma\not\!\!E_{\rm T}$ transverse mass in multi-body $\ell\gamma\not\!\!E_{\rm T}$ events. The points are CDF data, the hatched histogram is the total predicted mean background, and the cross-hatched histogram is the predicted mean diboson background.

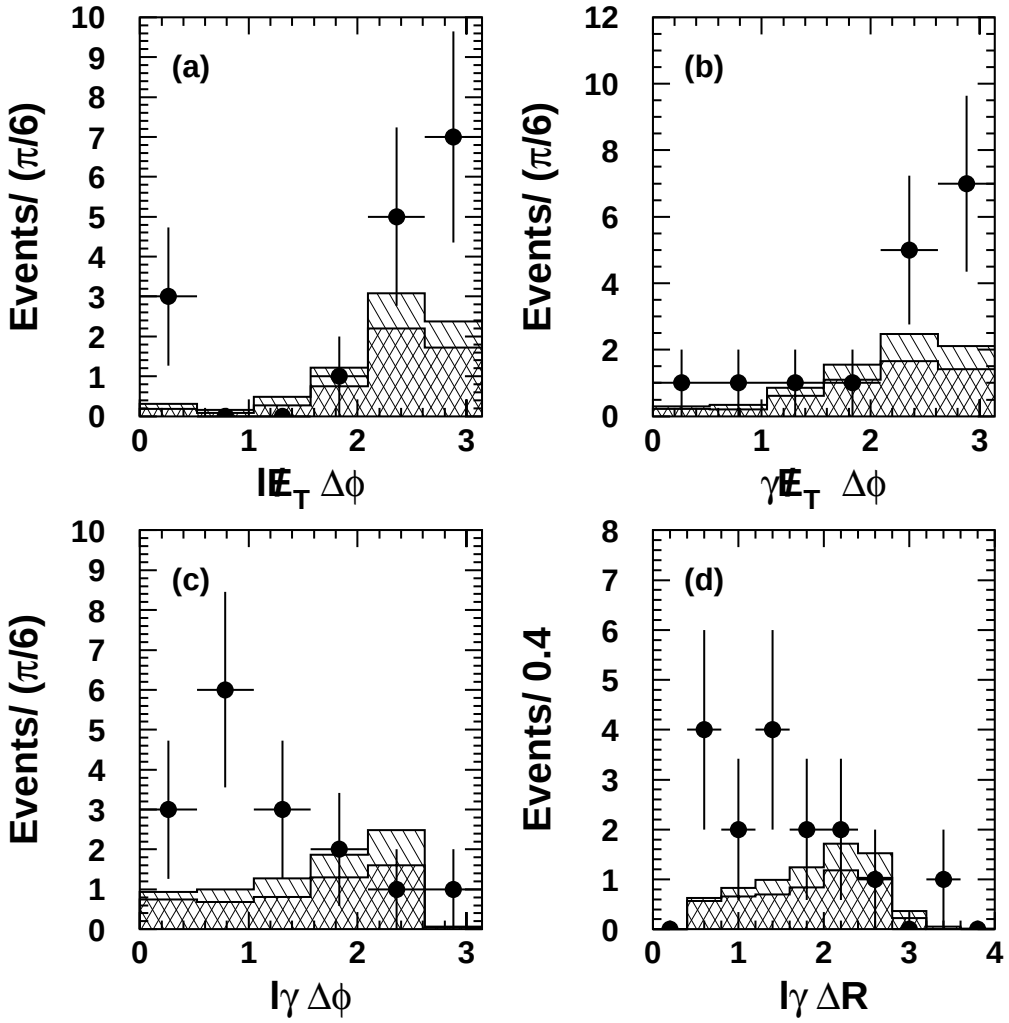

Figure 5.6: The distributions for (a) $\Delta\varphi(\ell \not\!\!E_{\rm T})$, (b) $\Delta\varphi(\gamma \not\!\!E_{\rm T})$, (c) $\Delta\varphi_{\ell\gamma}$, and (d) $\Delta R_{\ell\gamma}$ in multi-body $\ell\gamma \not\!\!E_{\rm T}$ events. The points are CDF data, the hatched histogram is the total predicted mean background, and the cross-hatched histogram is the predicted mean diboson background.

5.3 Events with Additional Leptons or Photons

The predicted and observed total rates for multi-body multi-lepton events are compared in Table 5.4. Nearly all of the predicted rate is expected from $Z^0\gamma$ production. A total of approximately 6 events are expected; 5 events are observed, including the $ee\gamma\gamma\not\!\!E_{\rm T}$ event. Both the electron and muon channels are in good agreement with the standard model. No $e\mu\gamma$ events were expected, and none were observed.

The predicted and observed total rates for multi-body multi-photon events are compared in Table 5.5. Only a small (0.01 event) rate is expected from $Z\gamma$ production; the single event observed is the $ee\gamma\gamma\not\!\!E_{\rm T}$ event. Judged solely as an event with one lepton with $E_T > 25$ GeV and two photons with $E_T > 25$ GeV, the upward fluctuation probability of this event is 1.5%. Judged as an event with an additional lepton and large $\not\!\!E_{\rm T}$, the upward fluctuation probability is much smaller, as described in a previous analysis [2].

Process	$ee\gamma$	$\mu\mu\gamma$	$\ell\ell\gamma$	$e\mu\gamma$
Z+γ	3.26 ± 0.44	2.19 ± 0.30	5.45 ± 0.61	0.05 ± 0.01
ℓ+jet, jet $\rightarrow \gamma$	0.19 ± 0.04	0.13 ± 0.03	0.32 ± 0.07	—
Mean Rate μ_{SM}	3.45 ± 0.44	2.32 ± 0.30	5.77 ± 0.61	0.05 ± 0.01
CDF Data N_0	4	1	5	0
$P(N \geq N_0 \mid \mu_{SM})$	0.45	—	—	—
$P(N \leq N_0 \mid \mu_{SM})$	—	0.33	0.61	0.95

Table 5.4: The mean rate μ_{SM} predicted by the standard model for multi-body events with additional leptons, the number N_0 observed in CDF data, and the one-sided fluctuation probability $P(N \geq N_0 \mid \mu_{SM})$. There exist correlated uncertainties between the different photon-lepton sources.

Process	$e\gamma\gamma$	$\mu\gamma\gamma$	$\ell\gamma\gamma$
Z+γ	0.012 ± 0.012	0.004 ± 0.004	0.016 ± 0.016
ℓ+jet, jet $\to \gamma$	—	—	—
Mean Rate μ_{SM}	0.012 ± 0.012	0.004 ± 0.004	0.016 ± 0.016
CDF Data N_0	1	0	1
$P(N \geq N_0 \mid \mu_{SM})$	0.013	~ 1	0.015

Table 5.5: The mean rate μ_{SM} predicted by the standard model for multi-body events with additional photons, the number N_0 observed in CDF data, and the one-sided fluctuation probability $P(N \geq N_0 \mid \mu_{SM})$. Expected contributions from jets misidentified as photons are negligible.

CHAPTER 6

CONCLUSION

We have performed an inclusive study of events containing at least one photon and one lepton (e or μ) in proton-antiproton collisions, motivated by the possibility of uncovering heretofore unobserved physical processes at the highest collision energies. In particular, the unexplained $ee\gamma\gamma\not{E}_{\rm T}$ event, uncovered early on in the CDF analysis of the 1994-5 run of the Fermilab Tevatron, indicated that the samples of previously unexamined particle combinations involving leptons and photons could contain potentially related, and therefore possibly novel, processes. The definition of the photon-lepton samples studied was chosen *a priori*, including the kinematic range of particles analyzed and the particle identification techniques employed. Wherever possible, the methods of previously published studies of leptons or photons at large transverse momentum were adopted. The questions of interest were also defined *a priori*, namely whether the total production rates of the photon-lepton subsamples enumerated in Figure 3.1 agree with standard model predictions. As a supplemental result, the distributions of the kinematic properties of the various photon-lepton subsamples are presented in Chapter 5 and the same properties are tabulated for each photon-lepton candidate in Appendix C.

The answers to those questions are as follows. A two-body photon-lepton sample, meant to encompass physical processes with two energetic particles in the final state, was observed to have a rate (33 events) consistent with that of standard model predictions (25 events). Specifically, the observed rate was greater then the mean predicted rate, but the probability of a statistical fluctuation of the mean predicted

rate up to or above the observed rate was more than 9%. A multi-body photon-lepton sample, meant to encompass physical processes with three or more energetic particles in the final state, was also observed to have an inclusive rate (27 events) consistent with standard model predictions (20 events). The observed rate was again higher than the mean predicted rate, but the probability of the fluctuation of the predicted rate up to or above the observed rate was 10%.

Several subsets of the multi-body photon-lepton sample were studied for the presence of additional particles. A subset of multi-body photon-lepton events with additional leptons (5 $ee\gamma$ or $\mu\mu\gamma$ events and 0 $e\mu\gamma$ events) was observed to have good agreement with standard model predictions (6 events and 0 events, respectively). A subset of multi-body photon-lepton events with additional photons was studied, yielding only the unexplained $ee\gamma\gamma\not{E}_{\rm T}$ event, whereas the predicted mean rate of inclusive $\ell\gamma\gamma$ events (regardless of the presence of $\not{E}_{\rm T}$ or a second lepton) is 0.01, a fluctuation probability of 1%. This event and estimations of its likelihood have been analyzed elsewhere [2].

Finally, a subset of the multi-body photon-lepton sample, consisting of those events with $\not{E}_{\rm T} > 25$ GeV, was observed to have a rate (16 events) that is substantially above the rate predicted by the standard model (7.6 ± 0.7 events). The probability of a statistical fluctuation of the mean predicted rate is 0.7%. Moreover, the excess rate in the observed inclusive multi-body photon-lepton sample can be completely accounted for by the excess in the multi-body $\ell\gamma\not{E}_{\rm T}$ sample; observed multi-body photon-lepton events with $\not{E}_{\rm T} < 25$ GeV agree well with the standard model.

That the standard model prediction yields the observed rate of a particular sample of events with 0.7% probability (equivalent to 2.7 standard deviations for a

Gaussian distribution) is an interesting result, but it is not a compelling observation of new physics. Multi-purpose particle physics experiments analyze dozens of independent samples of events, making a variety of comparisons with the standard model for each sample. In the context of this analysis alone, 5 mostly independent subsamples of photon-lepton events were analyzed. This large number of independent comparisons with the standard model for the same collection of data vastly increases the likelihood that outcomes with $\sim 1\%$ probability occur. However, once a particular comparison has been identified as anomalous, the same comparison performed with subsequent experiments is no longer subject to the dilution of its significance by the number of other independent comparisons performed concurrently. Hence an observation of equal or greater significance in the forthcoming run of the Fermilab Tevatron would confirm decisively the failure of the standard model to describe $\ell\gamma\not{E}_{\mathrm{T}}$ production; an observation of no significant excess would confirm the present result as a statistical fluctuation.

APPENDIX A

TRIGGER EFFICIENCY OF THE PHOTON-LEPTON SELECTION

A.1 Inclusive Photon Trigger Efficiency

As discussed in Chapter 3.1, the Level 1 trigger requirement for events in the inclusive photon sample is the presence of one or more CEM trigger towers with E_T exceeding 8 GeV. The efficiency of this Level 1 requirement has been measured to be $100^{+0.0}_{-0.3}\%$ for CEM clusters with E_T greater than 11 GeV [25]; it is therefore assumed that the Level 1 trigger efficiency for events in the inclusive photon sample is 100%.

There are two separate trigger paths through Level 2 and Level 3 for inclusive photon events. For events with photon E_T ranging from 25–55 GeV, a low-threshold, isolated photon trigger is required; for events with photon $E_T \geq 55$ GeV, a high-threshold trigger is required. The combined Level 2 $\times$ Level 3 efficiencies of these two trigger paths are measured separately.

The efficiency of the low-threshold, isolated photon trigger path, ϵ_{23}, is measured piecewise as follows: the efficiency of the E^{Iso}_{3x3} and CES trigger requirements, $\epsilon_{ISO,CES}$, is measured by comparing the low-threshold, isolated trigger with a photon trigger that has the same energy threshold but does not have the E^{Iso}_{3x3} and CES requirements; the efficiency of the cluster E_T threshold cut combined with the CES trigger requirement, $\epsilon_{E_T,CES}$, is measured by comparing the low-threshold, isolated photon trigger with an isolated photon trigger with a 10 GeV threshold; and the

efficiency of the CES requirement alone, ϵ_{CES}, is measured separately. The total efficiency of the low-threshold trigger is then given by:

$$\epsilon_{23} = \epsilon_{ISO,CES} \times \epsilon_{\mathrm{E_T},CES} \div \epsilon_{CES} \tag{A.1}$$

The total Level 2 $\times$ Level 3 efficiency of the low-threshold trigger, ϵ_{23}, is shown in Figure A.1 as a function of photon $\mathrm{E_T}$. Below 31 GeV, there exists significant photon $\mathrm{E_T}$ dependence, and trigger efficiency is modeled on a bin-by-bin basis in 1 GeV bins. Above 31 GeV, ϵ_{23} is flat with photon $\mathrm{E_T}$, and the trigger efficiency there is taken to be the average efficiency from 31 GeV to 55 GeV, $88.7 \pm 0.8\%$.

The high-threshold photon trigger has no Level 2 prerequisites, and at Level 3 requires only a fiducial CES cluster and an electromagnetic cluster with $\mathrm{E_T} >$ 50 GeV. The efficiency of this trigger for photons satisfying the cuts used in Table 3.1 has been measured to be $99.3^{+0.3}_{-0.4}\%$ for photon $\mathrm{E_T}$ above 55 GeV.

Figure A.2 summarizes the results of the trigger efficiency for events satisfying the photon cuts in Table 3.1. As photon $\mathrm{E_T}$ increases from 25 GeV to 31 GeV, the low-threshold, isolated photon trigger increases sharply in efficiency. From 31 GeV to 55 GeV, the efficiency of the low-threshold trigger is constant at 89%. Above 55 GeV, the high-threshold photon trigger is used, and the efficiency is constant at a higher value of 99%. Table A.1 lists the complete quantitative results, including uncertainties.

A.2 Photon-Muon Trigger Efficiency

Muon events and photon events have complementary trigger paths, neither of which is 100% efficient. It is therefore advantageous to require that photon-muon events

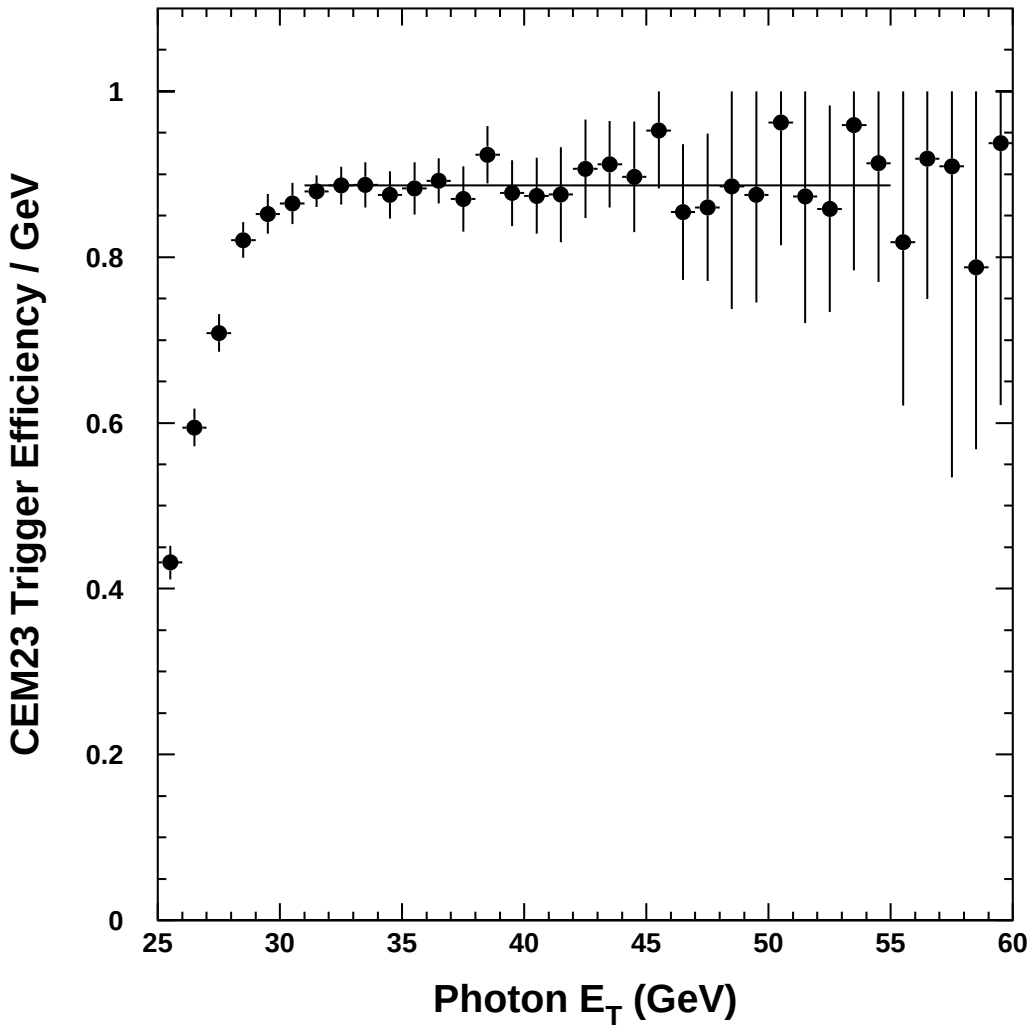

Figure A.1: The total efficiency of the low-threshold, isolated photon trigger, as a function of photon E_T, for events satisfying the cuts in Table 3.1. The points are CDF data; the horizontal line indicates the average efficiency of $88.7 \pm 0.8\%$ for 31 GeV $< E_T^{\gamma} <$ 55 GeV.

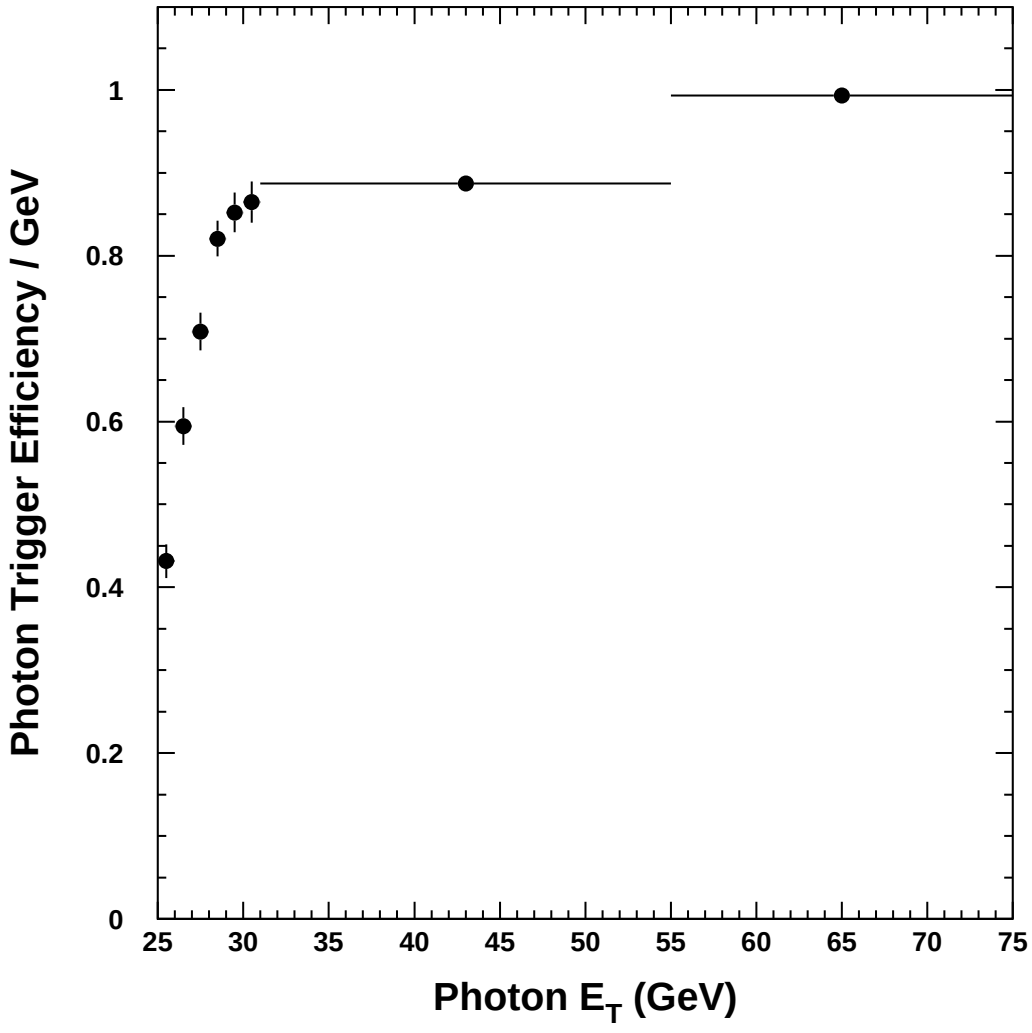

Figure A.2: The total inclusive photon trigger efficiency, as a function of photon E_T, for photons satisfying the cuts in Table 3.1.

Photon E_T (GeV)	Trigger Efficiency
25-26	0.431 ± 0.020
26-27	0.594 ± 0.023
27-28	0.708 ± 0.023
28-29	0.821 ± 0.022
29-30	0.852 ± 0.024
30-31	0.865 ± 0.025
31-55	0.887 ± 0.008
55-up	0.993 ± 0.004

Table A.1: Trigger efficiency of events satisfying the photon selection requirements in Table 3.1, as a function of photon E_T.

pass either a muon trigger path or a photon trigger path. To this end, the inclusive muon sample and the inclusive photon sample are combined to create the photon-muon data sample, and the combined efficiency for photon-muon events is the efficiency of the logical OR of the muon and photon triggers.

Level 2 muon triggers require either a CMUP muon stub, a CMNP muon stub, or a CMX muon stub which matches to a CTC track. The combined efficiency of the Level 1 and Level 2 muon triggers for CMUP or CMNP muons has been measured to be $86.3 \pm 3.0\%$; the corresponding CMX efficiency has been measured to be $69.6 \pm 5.0\%$. Inclusive muon triggers at Level 2 are prescaled; for photon-muon events a full scale Level 2 muon trigger is employed which requires a Level 2 calorimeter cluster with $E_T > 15$ GeV, the Level 2 "muon-jet trigger."

The probability that a photon with $E_T > 25$ GeV passes the 15 GeV jet trigger requirement is determined as follows. From the inclusive muon sample, events are selected which satisfy the following criteria: the event passes one of the Level 3 inclusive muon triggers described in Table 3.2, and the event passes the corresponding Level 2 trigger; there is exactly one fiducial CEM cluster with E_T >20 GeV, HAD/EM < 0.1, and isolation $E_T < 0.1 \times E_T$; and second calorimeter cluster with

$E_T > 10$ GeV. This results in a sample of 112 events; all of them also pass the appropriate muon plus jet trigger. The jet trigger efficiency for photon-muon events is therefore $100^{+0}_{-2}\%$. The muon plus jet triggers are not scaled, so the Level 1 $\times$ Level 2 efficiencies are simply the muon trigger efficiencies quoted above, 86.3% for CMUP-photon or CMNP-photon events and 69.6% for CMX-photon events.

At Level 3, the inclusive muon trigger (described in Table 3.2) corresponding to the appropriate Level 2 muon trigger is required. The Level 3 efficiency of the inclusive muon triggers has been measured to be $97.0^{+0.6}_{-0.7}\%$. The total trigger efficiency for photon-muon events from the inclusive muon sample is then simply the product of the Level 3 efficiency with the appropriate Level 1 $\times$ Level 2 efficiency: $83.7 \pm 3.4\%$ for CMNP-photon or CMUP-photon events, and $67.5 \pm 5.1\%$ for-CMX photon events.

The combined trigger efficiency of using both muon and photon triggers together is calculated as the logical OR of the two. Muon trigger efficiency varies by muon stub type (CMUP, CMNP, CMX, or other), and photon trigger efficiency varies by photon E_T, so the total trigger efficiency for photon-muon events with muon stub type μ_i and a given photon E_T is

$$\epsilon_{\mu\gamma}(\mu_i, E_T) = \epsilon_{\mu_i} + (1 - \epsilon_{\mu_i}) \times \epsilon_\gamma(E_T), \tag{A.2}$$

where $\epsilon_{CMUP} = \epsilon_{CMNP} = 83.7 \pm 3.4\%$, $\epsilon_{CMX} = 67.5 \pm 5.1\%$, $\epsilon_{other} = 0\%$, and $\epsilon_\gamma(E_T)$ is given in Table A.1.

The numbers used are given in Table A.2; the results are plotted in Figure A.3. It is observed that significant improvement over that of muon or photon triggers alone is obtained. The total uncertainty in the trigger efficiency of photon-muon events is taken to be $\pm 6\%$, which bounds the uncertainty for any muon type or photon E_T.

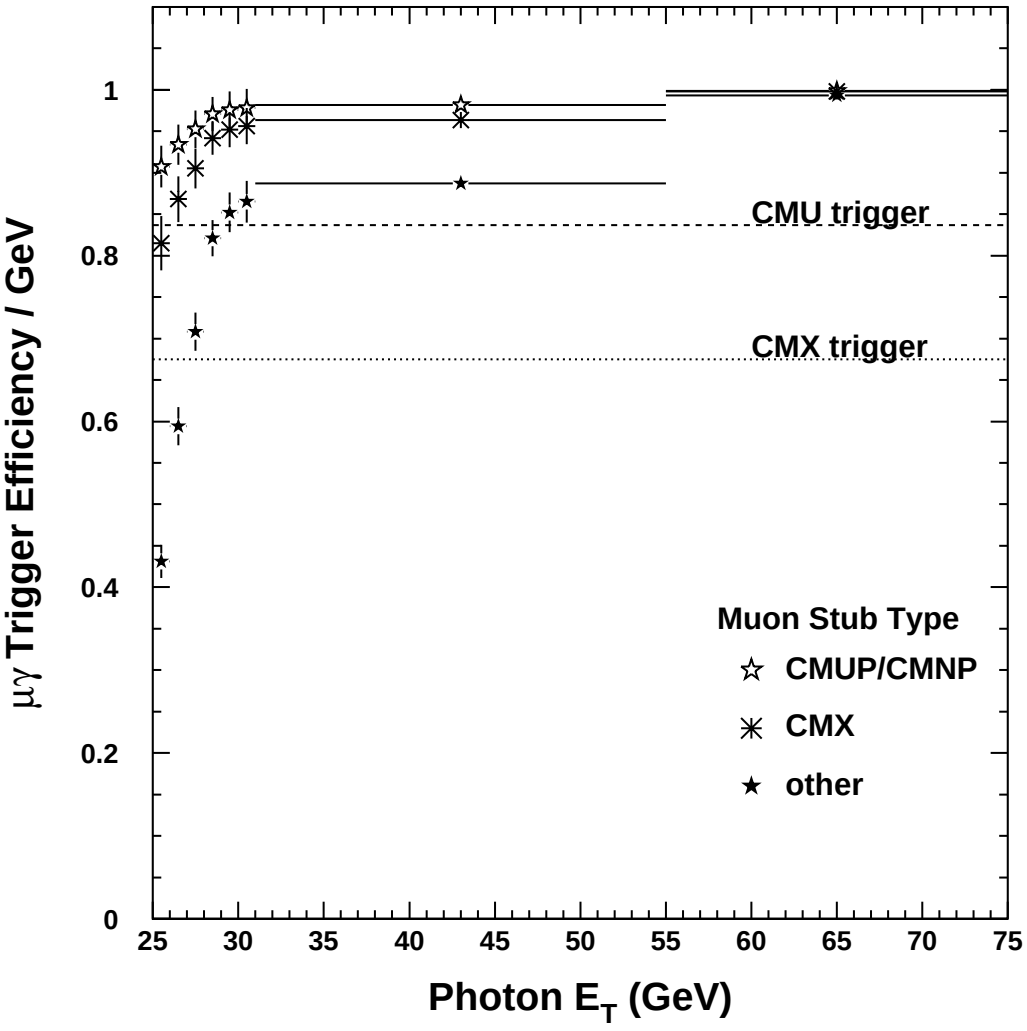

Figure A.3: The trigger efficiency of photon-muon events, as a function of photon E_T and muon stub type, for events satisfying all selection requirements. Included are the measurements for photon-muon events with CMUP or CMNP muons (unfilled stars), CMX muons (asterisks), or any other muon stub type (filled stars). The efficiencies of the CMUP/CMNP-jet triggers (dashed line) and the CMX-jet trigger (dotted line) are shown for comparison.

Muon Stub Type	CMUP/CMNP	CMX	any other
Photon E_T (GeV)			
25-26	0.907	0.815	0.431
26-27	0.934	0.868	0.594
27-28	0.952	0.905	0.708
28-29	0.971	0.942	0.821
29-30	0.976	0.952	0.852
30-31	0.978	0.956	0.865
31-55	0.982	0.963	0.887
55-up	0.999	0.998	0.993

Table A.2: The trigger efficiency for $\mu\gamma$ events satisfying all selection requirements, as a function of photon E_T and muon stub type.

A.3 Photon-Electron Trigger Efficiency

As discussed in Chapter 3.3, the Level 1 trigger requirement for events in the photon-electron sample is the presence of one or more CEM trigger towers with E_T exceeding 8 GeV. The efficiency of this Level 1 requirement is 100% (see Section A.1). At Level 2, two Level 2 CEM clusters with $E_T > 16$ GeV are required; the efficiency of this trigger has been measured in previous analyses [29] to be $100^{+0.0}_{-1.5}$% for two CEM clusters with E_T greater than 22 GeV; it is therefore assumed that the Level 2 efficiency for photon-electron events is 100%. At Level 3, the inclusive electron trigger described in Table 3.2 is required. The efficiency of this Level 3 trigger has been measured to be 98.5 ± 0.1% [25]. The overall trigger efficiency for photon-electron events is the product of the efficiencies of the 3 levels of triggers, equal to $98.5^{+0.1}_{-1.5}$%.

APPENDIX B

DETECTION EFFICIENCY OF PHOTON AND LEPTON SELECTION

This Appendix describes the measurements of the CDF detection efficiencies of the lepton and photon selection criteria described in Chapter 3. Measurements are made using both CDF data and data obtained from the simulation software described in Chapter 4.1, so that corrections to simulated particle identification efficiencies are obtained (Table 4.1). Many of the results have been measured in previous analyses; previously unpublished results are described here in detail.

B.1 Photon Identification Efficiency

Events are selected using a dielectron trigger requiring two or more CEM clusters with $E_T > 22$ GeV. A sample of events are then selected which pass this trigger and which have two central electron candidates consistent with Z^0 decay. Both candidates must have a well-matched track with momentum comparable to the electromagnetic shower energy, a fiducial CES cluster, and $E_T > 25$ GeV. The first candidate must satisfy all of the requirements in Table 3.1, appropriately modified for the presence of the electron track. The second candidate is not required to satisfy any of the photon shower requirements, but the invariant mass of the two electrons must lie within 5 GeV of the mass of the Z^0 boson. The complete set of requirements is listed in Table B.1. If P is the number of second candidates satisfying the requirements, and T is the total number of second candidates, then the photon detection

efficiency, ϵ_γ, is given by

$$\epsilon_\gamma = 2P/(T+P). \tag{B.1}$$

Table B.2 summarizes the results for each of the photon selection requirements. The total efficiency ϵ_γ is $86.0 \pm 0.7\%$.

The photon identification efficiency of simulated data is measured in an identical way. Using PYTHIA event generation and a CDF detector simulation, 250,000 $Z^0 \to e^+e^-$ events (approximately 1.2 fb^{-1}) were simulated and analyzed identically to the CDF $Z^0 \to e^+e^-$ data sample above, and the identification efficiencies computed are shown in Table B.2. Efficiencies of simulated data are systematically larger than that of CDF data. Any simulated data rate predictions should be corrected by a factor C_γ equal to the ratio of the photon identification efficiency measured in CDF data to that measured in simulation, with a systematic uncertainty given by $(1 - C_\gamma)/2$. C_γ, for various stages of selection, is shown in Table B.2. The appropriate correction for the complete photon selection criteria is $C_\gamma = 0.93 \pm 0.01(\text{stat}) \pm 0.04(\text{syst})$.

B.2 Lepton Identification Efficiency

The identification efficiency of the lepton selection criteria in Table 3.3, for both CDF data and simulated data, has been measured in previous analyses involving top quark production [30, 9]. The measurement technique is essentially identical to that described above, using samples of $Z^0 \to e^+e^-$ or $Z^0 \to \mu^+\mu^-$ events from CDF data and from simulated data to extract the relevant efficiencies. The set of efficiencies computed previously also includes those of the CMI muon criteria listed in Table 3.4.

First Electron Leg
CEM fiducial electron
$E_T > 25$ GeV
Electron Tracking Cuts
$p_T \times c > 5/9 \times E_T$
$\lvert\Delta x_{CES}\rvert < 1.5$ cm
$\lvert\Delta z_{CES}\rvert < 3$ cm
Electromagnetic Shower Cuts
Had/EM $< 0.055 + 0.00045 \times E^{\gamma}$
$\chi^2_{\rm Avg} < 20.0$
$E^{\rm CES}_{\rm 2nd} < 2.39 + 0.01 \times E^{\gamma}$ GeV
$\leq$1 (non-electron) tracks pointing at the cluster
0 (non-electron) tracks with $p_T > 1$ GeV
p_T of (non-electron) tracks in a cone of $0.4 < 5$ GeV/c
$E^{\rm Iso}_{\rm cone} < 2$ GeV
Second Electron Leg
First Leg Fiducial Cuts
$E_T > 25$ GeV
First Leg Electron Tracking Cuts
Electron track opposite in sign to First Leg
86 GeV $< M_{ee} <$ 96 GeV

Table B.1: The selection criteria for the dielectron sample from which the photon identification efficiency is computed.

The identification efficiency in CDF data of the selection criteria for LCEM, PEM, and FEM electrons listed in Table 3.4 has also been measured in previous analyses involving Z^0 production [13]; it remains here to measure the identification efficiency of these criteria for simulated data, where the methods of [13] are emulated.

The PYTHIA event generator program and a CDF detector simulation are used to create 250,000 $Z^0 \rightarrow e^+e^-$ events. Simulated events are selected which satisfy the following requirements: one central electron candidate satisfying the LCEM criteria in Table 3.4; a second fiducial electromagnetic energy cluster with E_T exceeding 20 GeV in the CEM, 15 GeV in the PEM, or 10 GeV in the FEM; and an invariant

Electromagnetic Shower Cuts, $E_T > 25$ GeV					
Criterion	Events (Data)	Eff. (%)	Events (MC)	Eff. (%)	$C_{\gamma\ ID}$
Sample	1648	100.0	19175	100.0	1.000
HAD/EM	1619	99.1	19068	99.7	.994
Track Cut	1486	94.8	18418	98.0	.968
2nd Cluster Cut	1442	93.3	17791	96.3	.970
$\chi^2_{\rm Avg} < 20.0$	1375	91.0	17314	94.9	.959
$\Sigma p_T < 5$ GeV	1362	90.5	17220	94.6	.956
$coriso < 2$ GeV	1244	86.0	16650	93.0	.926
$C_{\gamma\ ID}$ (per photon) $= 0.93 \pm 0.01 \pm 0.04$					

Table B.2: Identification efficiency of the electromagnetic shower requirements for the events satisfying the dielectron selection in Table 3.1. Included are the results for CDF $Z^0 \to e^+e^-$ events (Data), simulated $Z^0 \to e^+e^-$ events (MC), and the ratio of the two ($C_{\gamma\ ID}$).

mass of the two clusters within 15 GeV of M_Z. If P is the number of second LCEM electron candidates satisfying all LCEM selection requirements, and T is the total number of second LCEM candidates, then the LCEM electron detection efficiency is given by $2P/(T+P)$.

Similarly, if P is the number of PEM (or FEM) electron candidates satisfying all PEM (FEM) selection requirements, and T is the total number of PEM (FEM) candidates, then the PEM (FEM) detection efficiency is simply P/T. The measured identification efficiencies for various stages of selection are shown in Table B.3. It is observed that the $\chi^2_{3\times3}$ efficiency for PEM electrons is grossly underestimated by the simulation. This selection criterion is therefore not applied to simulated data, and simulated PEM electron candidates satisfying all other selection criteria are weighted by the $\chi^2_{3\times3}$ efficiency measured from CDF data (95%), in addition to the simulation correction factor for all other PEM selection criteria (94%).

Electron Identification Efficiency					
Criterion	Events (Data)	Eff. (%)	Events (MC)	Eff. (%)	$C_{e\ ID}$
LCEM electrons					
Sample	2762	100.0	28915	100.0	1.000
E/cp			28779	99.7	
HAD/EM			25064	92.9	
Isolation E_T	2263	88.9	24520	97.4	.913
PEM electrons					
Sample	2058	100.0	33855	100.0	1.000
HAD/EM	2033	98.8	33802	99.8	.990
Isolation E_T	1900	92.3	33360	98.5	.937
$\chi^2_{3\times3}$	1805	87.7	20833	61.7	1.416
FEM electrons					
Sample	271	100.0	5593	100.0	1.000
HAD/EM	265	97.8	5589	99.9	.979
Isolation E_T	205	75.4	5479	98.0	.769

Table B.3: Identification efficiency of the electron selection criteria in Table 3.4 for CDF data and simulated data. Included are the results for CDF $Z^0 \to e^+e^-$ events (Data), simulated $Z^0 \to e^+e^-$ events (MC), and the ratio of the two ($C_{e\ ID}$).

APPENDIX C

TABULATED PROPERTIES OF PHOTON-LEPTON CANDIDATES

	Photon			Lepton				$\not\!\!E_T$	
Run/event	E_T	φ	η	type	E_T	φ	η	$\not\!\!E_T$	φ
61124/197930	35.6	160	-0.65	CEM	34.9	337	-0.67	1.4	64
61221/ 7784	57.8	131	0.12	CEM	64.7	311	-0.38	7.8	147
63485/337978	34.9	273	-0.55	CEM	25.3	85	-0.67	23.2	139
64663/249519	32.5	173	0.65	CEM	31.6	355	-0.42	7.8	328
65004/150318	43.6	33	-0.42	CEM	45.2	205	0.57	19.5	27
65344/327956	52.2	32	-0.71	CEM	50.1	195	0.43	7.8	300
65426/226997	46.2	8	-0.02	CEM	44.4	199	-0.74	3.0	339
65750/125312	30.7	70	0.43	CEM	25.1	228	0.45	22.1	290
65917/ 27370	25.5	328	0.99	CEM	47.6	133	1.07	5.6	126
65974/ 26662	39.1	43	-0.85	CEM	41.7	233	-0.22	5.2	107
66208/ 13933	35.1	121	-0.65	CEM	27.0	288	0.56	3.5	273
66500/ 37841	44.7	190	-0.99	CEM	51.9	21	-0.64	6.3	244
66539/423756	38.2	176	-0.31	CEM	41.0	355	-0.48	2.9	106
68352/362020	40.4	148	-0.24	CEM	38.4	306	-0.26	13.7	13
68518/ 16652	56.9	347	-0.62	CEM	52.2	167	0.09	1.2	136
68570/429326	37.2	46	-0.72	CEM	39.3	245	-0.46	12.5	221
69005/ 62946	71.1	272	0.35	CEM	85.0	92	0.84	4.0	254
69709/299702	27.3	99	0.75	CEM	31.5	288	0.64	1.0	93
69833/ 6775	41.8	68	0.39	CEM	33.8	245	-0.45	3.9	272
70605/262312	35.6	191	-0.56	CEM	26.5	27	-0.60	6.1	50

Table C.1: The kinematic properties of photons, electrons, and $\not\!\!E_T$ in two-body photon-electron events. E_T and $\not\!\!E_T$ are given in units of GeV; φ is given in degrees.

	Photon			Lepton				$\vec{\not\!\!E}_T$
Run/event	E_T	φ	η	type	E_T	φ	η	$\not\!\!E_T$	φ
60573/ 40406	53.4	122	0.02	CMX	53.7	317	-0.80	13.6	224
64061/ 65839	47.6	173	-0.10	CMNP	39.5	10	0.64	7.4	272
64421/203383	44.7	247	-0.54	CMUP	42.0	66	-0.16	1.9	167
64934/125866	27.4	207	0.22	CMX	56.5	32	-0.93	18.9	86
65390/ 16199	48.3	79	0.59	CMUP	54.7	253	-0.30	38.4	127
65494/ 48066	28.9	46	-0.55	CMNP	44.1	213	-0.45	5.7	24
65894/ 15693	30.1	201	-0.71	CMP	27.8	1	-0.38	16.8	112
67494/700006	30.5	144	-0.58	CMNP	41.8	323	-0.56	14.3	152
67989/405914	25.8	121	0.12	CMNP	42.4	322	-0.26	35.0	134
68312/258160	31.0	268	0.22	CMP	44.9	104	-0.58	25.8	301
69036/ 49611	142.2	16	-0.85	CMUP	71.6	187	-0.33	64.4	229
70019/166983	39.2	27	0.68	CMUP	56.8	233	-0.45	25.1	84
70606/107771	45.5	339	-0.89	CMX	56.0	151	0.70	11.8	303

Table C.2: The kinematic properties of photons, muons, and $\not\!\!E_T$ in two-body photon-muon events. E_T and $\not\!\!E_T$ are given in units of GeV; φ is given in degrees.

	Photon			Lepton				$\not\!\!\vec{E}_T$	
Run/event	E_T	φ	η	type	E_T	φ	η	$\not\!\!E_T$	φ
56119/ 4309	34.9	335	-0.22	CEM	29.1	103	0.66	14.7	28
				LCEM	24.9	207	0.29		
61140/311478	54.2	223	0.03	CEM	26.5	275	-0.68	10.6	24
63149/ 4148	41.9	92	-0.22	CEM	33.2	125	-0.24	39.8	114
64345/ 8574	37.6	199	1.04	CEM	33.1	243	0.47	54.7	36
65085/273167	193.4	353	0.66	CEM	113.5	182	-0.23	1.0	273
				LCEM	85.8	157	0.54		
66347/268924	48.2	208	0.17	CEM	49.5	130	-1.07	7.2	274
66434/ 53860	27.6	28	-0.67	CEM	26.3	98	-0.24	37.4	243
67651/ 70517	31.0	102	0.12	CEM	52.1	79	0.26	106.3	64
68739/257646	36.2	332	-0.86	CEM	36.3	160	0.57	51.3	167
	32.3	246	-0.65	PEM	63.3	17	-1.72		
68915/158688	26.2	313	-0.75	CEM	46.6	136	-0.16	10.5	30
				PEM	25.7	285	1.19		
69831/ 56500	38.2	233	0.07	CEM	37.7	21	0.32	16.8	183
56934/ 62225	34.9	325	0.54	CMNP	30.5	259	0.05	47.9	112
58760/ 6610	32.8	262	0.47	CMUP	29.4	202	0.20	45.7	67
60972/ 72605	27.0	354	0.09	CMNP	25.3	322	0.27	43.6	163
61548/881820	36.4	6	-0.87	CMX	37.6	33	0.87	82.1	206
63078/ 25391	36.3	7	-0.40	CMUP	38.5	260	-0.33	4.2	294
65277/541087	25.3	351	-0.59	CMX	41.7	221	0.63	39.5	59
65472/195753	27.0	326	0.81	CMNP	30.3	278	-0.36	54.0	120
65769/ 1449	26.3	107	-0.39	CMNP	44.8	83	-0.07	26.5	248
66209/ 15413	46.2	211	0.65	CMUP	32.3	127	-0.17	55.0	357
66411/475700	29.5	101	-0.67	CMUP	57.3	39	-0.17	21.7	75
67737/298286	26.9	304	0.96	CMX	39.1	61	0.94	39.8	204
67862/355699	29.9	67	0.19	CMX	26.1	31	-0.92	49.9	223
69464/118013	35.1	142	0.70	CMUP	47.0	352	0.07	12.8	220
69998/ 73762	43.1	162	0.96	CMUP	39.4	56	-0.18	41.8	296
70577/406481	38.7	303	0.25	CMUP	45.3	181	-0.12	2.1	73
				CMX	34.4	34	0.81		
70605/776306	25.1	4	-0.53	CMUP	64.4	144	0.26	14.0	256

Table C.3: The kinematic properties of photons, leptons, and $\not\!\!E_T$ in inclusive multi-body photon-lepton events. E_T and $\not\!\!E_T$ are given in units of GeV; φ is given in degrees.

	Photon				Lepton			$\not\!\!E_T$	
Run/event	E_T	φ	η	type	E_T	φ	η	$\not\!\!E_T$	φ
63149/ 4148	41.9	92	-0.22	CEM	33.2	125	-0.24	39.8	114
64345/ 8574	37.6	199	1.04	CEM	33.1	243	0.47	54.7	36
66434/ 53860	27.6	28	-0.67	CEM	26.3	98	-0.24	37.4	243
67651/ 70517	31.0	102	0.12	CEM	52.1	79	0.26	106.3	64
68739/257646	36.2	332	-0.86	CEM	36.3	160	0.57	51.3	167
	32.3	246	-0.65	PEM	63.3	17	-1.72		
56934/ 62225	34.9	325	0.54	CMNP	30.5	259	0.05	47.9	112
58760/ 6610	32.8	262	0.47	CMUP	29.4	202	0.20	45.7	67
60972/ 72605	27.0	354	0.09	CMNP	25.3	322	0.27	43.6	163
61548/881820	36.4	6	-0.87	CMX	37.6	33	0.87	82.1	206
65277/541087	25.3	351	-0.59	CMX	41.7	221	0.63	39.5	59
65472/195753	27.0	326	0.81	CMNP	30.3	278	-0.36	54.0	120
65769/ 1449	26.3	107	-0.39	CMNP	44.8	83	-0.07	26.5	248
66209/ 15413	46.2	211	0.65	CMUP	32.3	127	-0.17	55.0	357
67737/298286	26.9	304	0.96	CMX	39.1	61	0.94	39.8	204
67862/355699	29.9	67	0.19	CMX	26.1	31	-0.92	49.9	223
69998/ 73762	43.1	162	0.96	CMUP	39.4	56	-0.18	41.8	296

Table C.4: The kinematic properties of photons, leptons, and $\not\!\!E_T$ in multi-body photon-lepton events with $\not\!\!E_T > 25$ GeV. E_T and $\not\!\!E_T$ are given in units of GeV; φ is given in degrees.

REFERENCES

[1] F. Abe *et al.*, Nucl. Instrum. Methods Phys. Res., Sect. A **271**, 387 (1988). The CDF coordinate system defines r, ϕ, and z as cylindrical coordinates, with the z-axis along the direction of the proton beam. The angle θ is the polar angle relative to the z-axis, the pseudorapidity is defined as $\eta = -\ln(\tan(\theta/2))$, and the transverse energy is defined as $E_T = E\sin\theta$. Missing transverse energy ($\not\!\!E_T$) is the vector opposite to the vector sum of the transverse energies of all objects in an event, $\not\!\!E_T = -\Sigma E_T$.

[2] D. Toback, Ph. D. thesis, University of Chicago, 1997.

[3] S. Ambrosanio, G. L. Kane, G. D. Kribs, S. P. Martin, and S. Mrenna, Phys. Rev. Lett. **76**, 3498 (1996); G. L. Kane and S. Mrenna, Phys. Rev. Lett. **77** 3502 (1996); S. Ambrosanio, G. L. Kane, G. D. Kribs, S. P. Martin, and S. Mrenna, Phys. Rev. D **55**, 1372 (1997).

[4] B. Abbott *et al.*, Phys. Rev. Lett. **82**, 2244 (1999); F. Abe *et al.*, Phys. Rev. D **59**, 092002 (1999); B. Abbott *et al.*, Phys. Rev. Lett. **80**, 442 (1998); B. Abbott *et al.*, Phys. Rev. Lett. **81**, 524 (1998); F. Abe *et al.*, Phys. Rev. Lett **81**, 1791 (1998); P. J. Wilson, in *ICHEP 98*, Proceedings of the 29th International Conference in High-energy Physics, Vancouver, Canada, 1998, edited by A. Astbury, D. Axen and J. Robinson (World Scientific, Singapore, 1998); S. Abachi *et al.*, Phys. Rev. Lett. **78**, 2070 (1997).

[5] B. Abbott *et al.*, Phys. Rev. Lett. **82**, 29 (1999).

[6] F. Abe *et al.*, Phys. Rev. Lett **83**, 3124 (1999).

[7] F. Snider *et al.*, Nucl. Instrum. Methods **A268**, 75 (1988). This is the reference for the previous generation of the device. The replacement for the 1994-5 data sample has more modules, each with a shorter drift length but is otherwise similar.

[8] G. W. Foster *et al.*, Nucl. Instrum. Methods Phys. Res. A **268**, 33 (1988).

[9] T. Affolder *et al.*, Report No. FERMILAB-PUB-00-127-E (2000); F. Abe *et al.*, Phys. Rev. D **50**, 2966 (1994).

[10] F. Abe *et al.*, Phys. Rev. D **59**, 092002 (1999); Phys. Rev. Lett **83**, 3124 (1999).

[11] T. Affolder *et al.*, Report No. FERMILAB-PUB-00-158-E (2000); F. Abe *et al.*, Phys. Rev. D **52**, 4784 (1995).

[12] Trigger towers subtend 0.2 in η by 15° in ϕ.

[13] J. Wahl, Ph. D. thesis, University of Chicago, 1999; F. Abe *et al.*, Phys. Rev. D **52**, 2624 (1995); S. Kopp, Ph. D. thesis, University of Chicago, 1994.

[14] F. Abe *et al.*, Phys. Rev. D **45**, 1448 (1992).

[15] F. Abe *et al.*, Phys. Rev. D **59**, 092002 (1999); **52**, 2624 (1995); J. Wahl, Ph. D. thesis, University of Chicago, 1999; D. Toback, Ph. D. thesis, University of Chicago, 1997; S. Kopp, Ph. D. thesis, University of Chicago, 1994.

[16] The source code is available publicly at *http://www.hep.anl.gov/theory/mrenna/sources/uli.uu*.

[17] U. Baur and E. L. Berger, Phys. Rev. D **47**, 4889 (1993); **41**, 1476 (1990).

[18] T. Sjostrand, Computer Physics Commun. **82** (1994) 74; S. Mrenna, Computer Physics Commun. **101** (1997) 232. An archive of program versions and documentation is available publicly at *http://www.thep.lu.se/tf2/staff/torbjorn/Pythia.html*.

[19] H. L. Lai *et al.*, Eur. Phys. J. C **12**, 375 (2000). The source code is available publicly at *http://www.phys.psu.edu/~cteq/CTEQ5Table/*.

[20] TAUOLA version 2.5 (June 1994), S. Jadach *et al.*, Computer Phys. Commun. **76** 361 (1993).

[21] A.D. Martin, R.G. Roberts, W.J. Stirling, and R.S. Thorne, Eur. Phys. J. C **4**, 463 (1998). A 5% uncertainty is recommended for W and Z^0 boson production at the Tevatron. The parton species and momenta contributing to $W\gamma$ and $Z^0\gamma$ production are very similar.

[22] U. Baur, T. Han, and J. Ohnemus, Phys. Rev. D **57** (1998) 2823; U. Baur, T. Han, and J. Ohnemus, Phys. Rev. D **48** (1993) 5140; J. Ohnemus, Phys. Rev. D **47** (1993) 940.

[23] F. Abe *et al.*, Phys. Rev. D **59**, 092002 (1999).

[24] D. Cronin-Hennessy *et al.*, Nucl. Instrum. Methods Phys. Res., Sect. A **443/1**, 37-50 (2000).

[25] J. Wahl, Ph.D. thesis, University of Chicago, 1999.

[26] J. Yu, Report No. FERMILAB-CONF-98-198-E (1998); J.W. Cronin *et al.*, Phys. Rev. Lett. **38**, 115 (1977); Phys. Rev. **D11**, 3105 (1975).

[27] QQ version 8.08 (June 1991), P. Avery, K. Read, G. Trahern, Cornell Inernal Report No. CSN-212 (1985), unpublished.

[28] S. Kuhlmann, Report No. FERMILAB-CONF-99-165-E (1998); F. Abe *et al.*, Phys. Rev. D **60**, 092003 (1999); Phys. Rev. Lett. **77**, 5005 (1996); R. Hamilton, Ph.D.thesis, Harvard University, 1996.

[29] D. Toback, Ph.D. thesis, University of Chicago, 1997, p.29.

[30] M. Kruse, Ph.D. thesis, Purdue University, 1996.